Lithofacies and depositional setting of a highly prospective lacustrine shale oil succession from the Upper Cretaceous Qingshankou Formation in the Gulong sag, northern Songliao Basin, northeast China

Bo Liu, Haoli Wang, Xiaofei Fu, Yunfeng Bai, Longhui Bai, Mengcheng Jia, and Bo He

ABSTRACT

The lacustrine shale of the Upper Cretaceous Qingshankou Formation is the principal prospective unconventional target lithology, acting as source, reservoir, and seal. Lithofacies and associated storage capacity are two significant factors in shale oil prospectivity. This paper describes an investigation of the lower Qingshankou Formation lacustrine shale based on detailed description and analysis of cores, shale lithofacies characteristics, depositional setting, and stacking patterns.

Seven lithofacies are recognized based on organic matter content, sedimentary structure, and mineralogy, all exhibiting rapid vertical and lateral changes controlled by the depositional setting and basin evolution. An overall trend from shallow-water to deep-water depositional environments is interpreted from the characteristics of the infilling sequences, characterized by increasing total organic carbon (*TOC*) and total clay content and decreasing layer thickness (i.e., from bedded to laminated then to massive sedimentary structures). Periods of deposition during shallowing cycles show a reverse trend in the sedimentary characteristics described above. The sedimentary rocks in the studied interval show three complete short-term cycles, each one containing progressive and regressive system tracts.

Manuscript received December 18, 2017; provisional acceptance February 26, 2018; revised manuscript received March 30, 2018; revised manuscript provisional acceptance April 19, 2018; 2nd revised manuscript received May 11, 2018; final acceptance August 3, 2018.
DOI:10.1306/08031817416

AUTHORS

Bo Liu ~ *Accumulation and Development of Unconventional Oil and Gas, State Key Laboratory Cultivation Base (jointly constructed by Heilongjiang Province and Ministry of Science and Technology), Northeast Petroleum University, Daqing, China; State Key Laboratory of Oil and Gas Reservoir Geology and Exploitation, Chengdu University of Technology, Chengdu, China; present address: Department of Earth Science, Northeast Petroleum University, Daqing, China; liubo@nepu.edu.cn*

Bo Liu received his Ph.D. from the China University of Petroleum in 2011 and is now a professor at Northeast Petroleum University. His current interests include the development of lacustrine source rocks and shale oil potential in lacustrine basins.

Haoli Wang ~ *Accumulation and Development of Unconventional Oil and Gas, State Key Laboratory Cultivation Base (jointly constructed by Heilongjiang Province and Ministry of Science and Technology), Northeast Petroleum University, Daqing, China; State Key Laboratory of Oil and Gas Reservoir Geology and Exploitation, Chengdu University of Technology, Chengdu, China; 935655809@qq.com*

Haoli Wang is now a master's degree candidate under the guidance of Bo Liu at Northeast Petroleum University. Her current interests include the development of lacustrine source rocks and shale oil potential in lacustrine basins.

Xiaofei Fu ~ *Accumulation and Development of Unconventional Oil and Gas, State Key Laboratory Cultivation Base (jointly constructed by Heilongjiang Province and Ministry of Science and Technology), Northeast Petroleum University, Daqing, China; fuxiaofei2008@sohu.com*

Xiaofei Fu received his Ph.D. from the Research Institute of Petroleum Exploration and Development, PetroChina, in 2007 and is now a professor at Northeast Petroleum University. His current interests include shale oil potential and fault sealing.

YUNFENG BAI ~ *PetroChina Daqing Oilfield Company, Daqing, China; 84478917@qq.com*

Yunfeng Bai received his Ph.D. from Jilin University in 2008. He is currently working as an exploration geologist at PetroChina Daqing Oilfield Company.

LONGHUI BAI ~ *Accumulation and Development of Unconventional Oil and Gas, State Key Laboratory Cultivation Base (jointly constructed by Heilongjiang Province and Ministry of Science and Technology), Northeast Petroleum University, Daqing, China; State Key Laboratory of Oil and Gas Reservoir Geology and Exploitation, Chengdu University of Technology, Chengdu, China; 1021864364@qq.com*

Longhui Bai is now a master's degree candidate under the guidance of Bo Liu at Northeast Petroleum University. His current interests include the development of lacustrine source rocks and shale oil potential in lacustrine basins.

MENGCHENG JIA ~ *PetroChina Daqing Oilfield Company, Daqing, China; 826146281@qq.com*

Mengcheng Jia received her B.S. degree from Northeast Petroleum University in 2017. She is currently working as an exploration geologist at PetroChina Daqing Oilfield Company.

BO HE ~ *PetroChina Daqing Oilfield Company, Daqing, China; 420630591@qq.com*

Bo He received her B.S. degree from Northeast Petroleum University in 2017. She is currently working as an exploration geologist at PetroChina Daqing Oilfield Company.

ACKNOWLEDGMENTS

This study was supported by Open Fund of the State Key Laboratory of Oil and Gas Reservoir Geology and Exploitation (Chengdu University of Technology, PLC20180402) and the National Natural Science Foundation of China (nos. 41472125, U1562214), which are gratefully acknowledged. Thanks also to the University Nursing Program for Young Scholars with Creative Talents in Heilongjiang Province (UNPYSCT-2015077,

Massive siliceous mudstones with both high and moderate *TOC* are considered to have the best hydrocarbon generation potential. Laminated siliceous mudstones, bedded siltstones, and calcareous mudstones with moderate and low *TOC* could have the same high hydrocarbon saturations as the high-*TOC* massive siliceous mudstones, but these lithologies contain more brittle minerals than the massive mudstones. Several siltstone samples show low or zero saturation of in situ hydrocarbons; this is considered to be related to a combination of fair to poor hydrocarbon generation potential and extremely low permeability, limiting migration. Moderate-*TOC* laminated siliceous mudstones were also observed to have connective pore-fracture networks. It can be demonstrated that successive thick sequences of moderate-*TOC* laminated siliceous mudstones, showing high volumes of hydrocarbon in situ, a high mineral brittleness index, and good permeability, combine to form shale oil exploration "sweet spots."

INTRODUCTION

The Songliao Basin, covering an area of 260,000 km^2 (100,000 mi^2), is one of the largest continental Cretaceous basins in the world and hosts the largest oil field in China, containing abundant conventional hydrocarbon resources (Xu et al., 2015). The Upper Cretaceous Qingshankou and Nenjiang shales are the most prolific source rocks in the Songliao Basin (Bechtel et al., 2012). Although commonly called "shales," these organic mudstones (Aplin and Macquaker, 2011) are specifically defined as fine-grained sedimentary rocks with elevated total organic carbon (*TOC*) that contain clay-sized particles (<4 μm), with variable amounts of silt-sized floating grains (up to 62.5 μm) of biogenic and detrital origin. Organic mudstones are highly heterogeneous and have a complex inorganic mineralogy that varies vertically and laterally at different scales (Macquaker and Adams, 2003). The term "lithofacies," as defined by Eberzin (1940), is the basic unit that constitutes a shale reservoir, reflecting an integration of all the important lithologic features of sedimentary rocks, such as mineral composition, organic matter content, rock texture, sedimentary structure, bedding, color, size distribution, roundness, and sorting (Dill et al., 2005). The global success of shale oil exploration shows that the lithofacies characterization is an effective and significant approach to allow understanding of the accumulation of organic matter, depositional processes, chemical characteristics of the water column, and most importantly, identification of favorable reservoir intervals (Loucks and Ruppel, 2007; Wang and Carr, 2012; Newport et al., 2016; Tang et al., 2016).

Contributing to the worldwide growth in production of unconventional oil and gas, tight oil has also been discovered in the sandstones of the second and third members of the Qingshankou

Formation (K_2qn^{2+3}) in the Songliao Basin (Shi et al., 2015). The Qingshankou Formation contains shale oil layers with high *TOC* and high oil yield near the base of its first (lower) member (K_2qn^1; Feng et al., 2011). For this reason, over the past two decades, high-resolution studies of the potential for hydrocarbon generation and the reconstruction of paleoenvironmental changes have been undertaken (Zhou and Littke, 1999; Jia et al., 2013b; Xu et al., 2015). In recent years, excellent examples of shale oil potential from organic matter–rich shales of the first member of the Qingshankou Formation have caused researchers to focus on the reservoir characteristics of this lacustrine deep-water sedimentary sequence (Liu et al., 2014a; Shi et al., 2015). In the northern part of the Songliao Basin, the key factor affecting the potential of shale oil within deeply buried shales (>1700 m [>5600 ft]) is considered to be the heterogeneity of the lithofacies (Cao et al., 2017). Detailed information about the mineralogy and lithology of this lacustrine, fine-grained sedimentary sequence is required to understand the relationships between organic matter enrichment, lithofacies variations, and basin evolution within the Qingshankou Formation. Systematic studies of lithofacies changes during basin evolution are currently lacking because until now the Qingshankou Formation has been considered simply as a homogenous hydrocarbon source rock. To fill this gap, the focus of this paper is the investigation of the organic geochemistry, mineralogy, and lithology of the first member of the Qingshankou Formation. It is hoped that further insights into shale oil exploration strategies will arise from this data on the distribution and heterogeneity of lithofacies within these Cretaceous strata.

The aim of this study is to scientifically classify shale lithofacies based on sample descriptions and the analysis of mineralogical properties and organic geochemistry. Subsequently, the aim is to investigate the characteristics of each shale lithofacies within the first member of the Qingshankou Formation and its position in the sedimentary sequences deposited during the evolution of the Songliao Basin. The results obtained are important to the study of the sedimentary processes and geological setting of organic-rich shales, providing detailed insights into the characteristics of shale reservoirs.

REGIONAL SETTING

The Songliao Basin, located in northeastern China, is a large north–northeast-trending Mesozoic–Cenozoic continental lacustrine basin (Figure 1). Three major tectonic episodes occurred during the evolution of the basin: fault-related subsidence, thermal subsidence, and finally inversion. The basin contains structures relating to both the Jurassic fault-related subsidence and post-Jurassic thermal subsidence. Basement rocks consist of

QC2015043) and the National Basic Research Program of China (2016ZX05003-002) for financial support. Samples were provided by the PetroChina Daqing Oil Company.

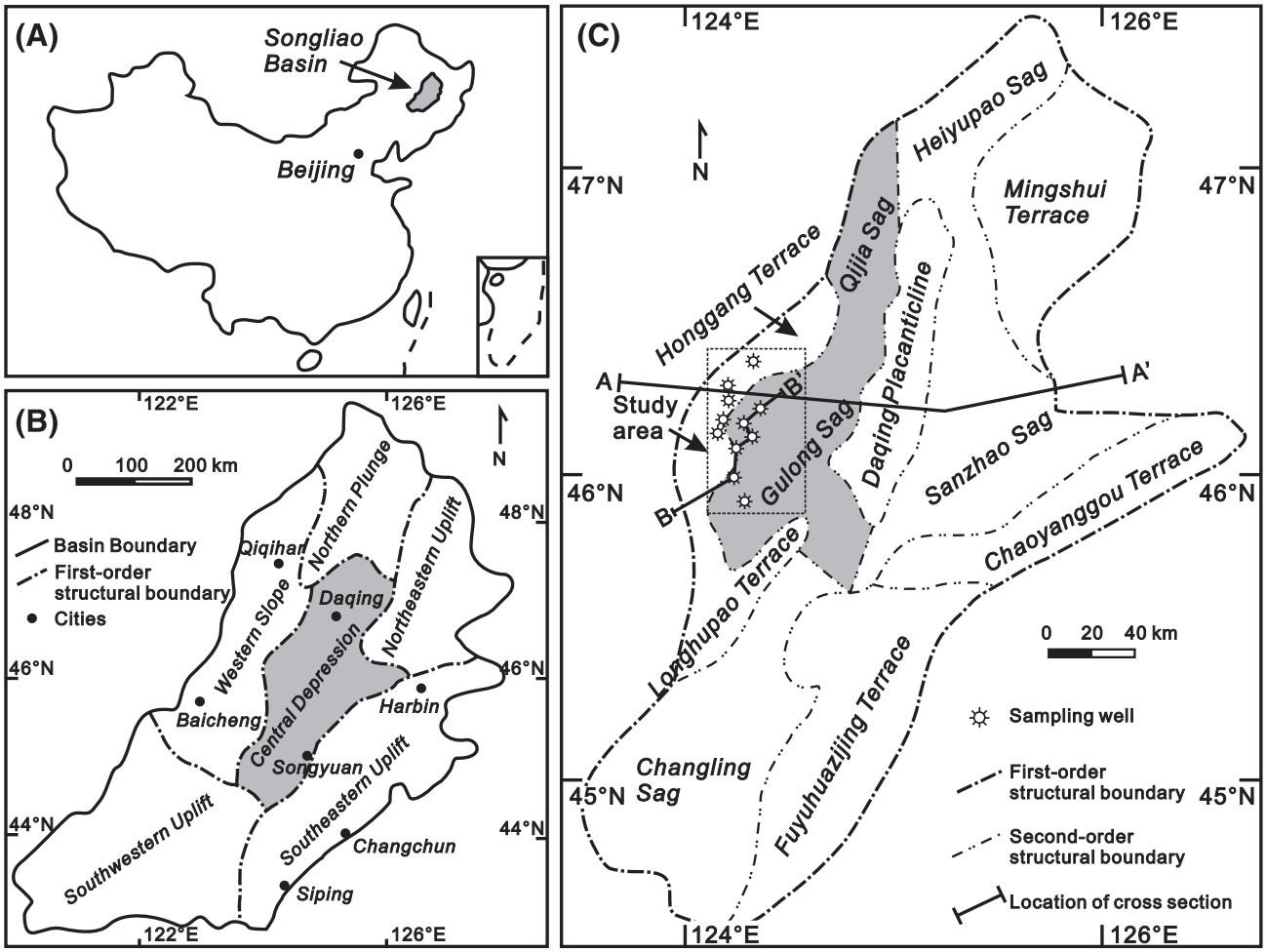

Figure 1. Generalized map showing the location of the Songliao Basin (A), central depression (B), study area (Gulong sag), the location of cores, and the cross section (C).

Paleozoic metamorphic, volcanic, and magmatic rocks (Figure 2; Feng et al., 2010).

During the Cretaceous rifting stage, the Pacific plate began to subduct below the Asian continent, forming a series of fault-bounded basins in northeastern China as the center of tectonic activity migrated. In the middle Cretaceous, the lithosphere gradually cooled, resulting in extensive thermal subsidence of the basin with a corresponding increase in basin aerial extent (P. Wang et al., 2016). The central highlands eventually formed the central depression because of a strong thermal equilibrium adjustment in the underlying mantle. After the deposition of the Nenjiang Formation, the deep structure of the basin continued to undergo equilibrium adjustment (Zhao et al., 2013, 2015). The lake basin gradually shrank, and the Songliao Basin was inverted by folding and uplift (Wei et al., 2010). Based on regional tectonics, the basin can be subdivided into six tectonic units: western slope, northern plunge, central depression, northeastern uplift zone, southeastern uplift zone, and southwestern uplift zone (Figure 1B).

Jurassic, Cretaceous, and Cenozoic sedimentary rocks with a maximum thickness of 7000 m (23,000 ft) developed on the basement. Cretaceous sedimentary rocks are widely distributed beneath Cenozoic deposits. Three regional angular unconformities separate the basin fill into three tectono-stratigraphic sequences: the synrift stage, corresponding to the Lower Cretaceous Huoshiling, Shahezi, and Yingcheng Formations; the postrift stage, which includes the Lower Cretaceous Denglouku and Quantou Formations and Upper Cretaceous Qingshankou, Yaojia, and Nenjiang Formations; and the structural inversion stage, which includes the Sifangtai and Mingshui Formations (P. Wang et al., 2016). Of these,

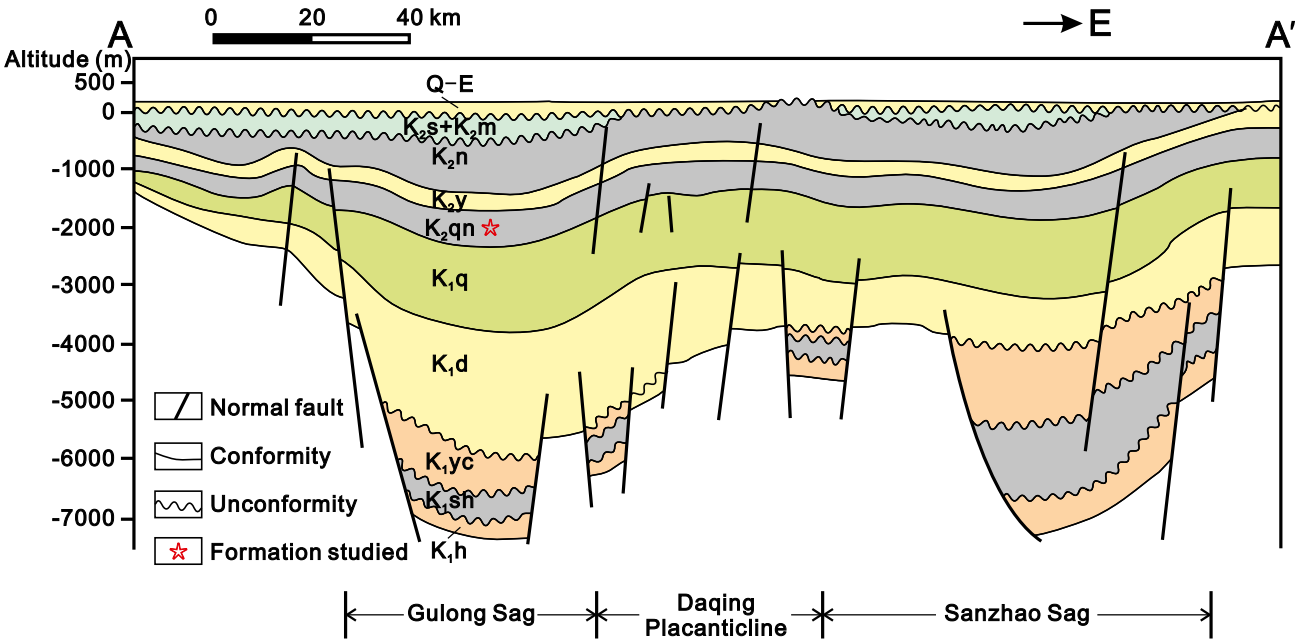

Figure 2. Transverse section across the middle segment of the Gulong sag, Daqing placanticline, and Sanzhao sag. E = Paleogene; K_1d = Lower Cretaceous Denglouku Formation; K_1h = Lower Cretaceous Huoshiling Formation; K_1q = Lower Cretaceous Quantou Formation; K_1sh = Lower Cretaceous Shahezi Formation; K_1yc = Lower Cretaceous Yingcheng Formation; K_2m = Upper Cretaceous Mingshui Formation; K_2n = Upper Cretaceous Nenjiang Formation; K_2qn = Upper Cretaceous Qingshankou Formation; K_2s = Upper Cretaceous Sifangtai Formation; K_2y = Upper Cretaceous Yaojia Formation; Q = Quaternary.

the Qingshankou and Nenjiang Formations are the major petroleum source beds (Bechtel et al., 2012).

The Qingshankou Formation (K_2qn) was deposited in a moderately deep lake setting influenced by periodic marine incursion events during a period of global sea-level rise (Liu et al., 1993; Huang et al., 2013). It is subdivided into three members (K_2qn^1, K_2qn^2, and K_2qn^3) based on lithology (Figure 3). The first member of the Qingshankou Formation (K_2qn^1), one of the most favorable source rocks in the Songliao Basin, is widely distributed across the basin and is only disrupted on the western edge of the basin. It is up to 500 m (1600 ft) thick, and it developed during a rapid, large-scale lake transgression. Several lake-level rises occurred during the deposition of K_2qn^1 related to stepwise subsidence of the basement (Zhong and Yang, 1978), resulting in deposition of thick, dark-gray mudstones and shales interbedded with fine-grained siltstones. This member was selected as the target layer for this study. The second member of the Qingshankou Formation (K_2qn^2) was deposited during a period of lake regression.

The Gulong sag, located in the western part of the central depression, remained a focus for deposition and subsidence during the deposition of the Qingshankou Formation. This formation consists of highly variable nearshore shallow lacustrine and semideep to deep lacustrine facies and was selected as the focus area of this study (Figure 1C).

METHODS

Sample Collection and Analysis

All 42 samples of the target layers were obtained from 11 drill cores acquired along the western slope of the Gulong sag and include all facies, from nearshore shallow to deep lacustrine (Figure 1C). Bulk geochemical and mineralogical analyses were performed on all samples.

The *TOC* was determined using an Eltra Helios CS elemental analyzer. Samples were pretreated with phosphoric acid to remove carbonates (B. Liu et al., 2017). Pyrolysis was performed using a Rock-Eval 6 analyzer to obtain the amount of free hydrocarbon in the sample (S_1), the amount of pyrolyzate released from kerogen (S_2), and the temperature of maximum hydrocarbon generation (T_{max}). The S_2 was normalized by the *TOC* value to give the hydrogen

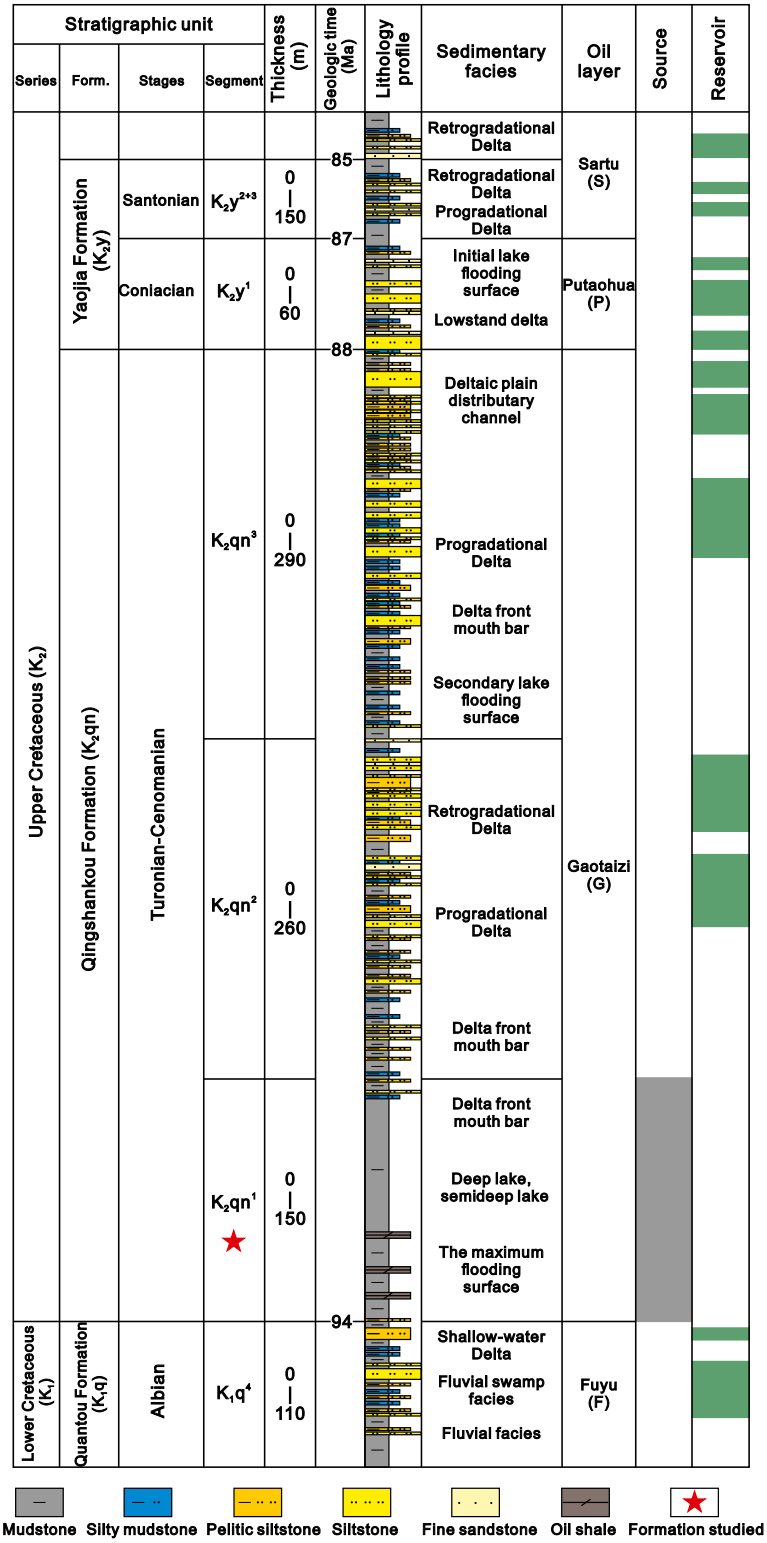

Figure 3. General lithologic stratigraphy of the Qingshankou Formation (Form.) in northern Songliao Basin. Gray and green in the column show the source and reservoir successions, respectively. K_1q^4 = the fourth member of Quantou Formation; K_2qn^1 = the first member of the Qingshankou Formation; K_2qn^2 = the second member of the Qingshankou Formation; K_2qn^3 = the third member of the Qingshankou Formation; K_2y^1 = the first member of Yaojia Formation; K_2y^{2+3} = the second and third members of Yaojia Formation.

index (*HI*). Serving as a maturity indicator, T_{max} is defined at the value of the S_2 peak (Langford and Blanc-Valleron, 1990). Finally, the production index (*PI*) and oil saturation index (*OSI*) parameters were determined for each sample: $PI = S_1/(S_1 + S_2)$; $OSI = S_1/TOC \times 100$ (Jarvie, 2012).

The x-ray diffraction (XRD) analysis was performed to obtain semiquantitative mineralogical data using a Bruker D8 Advance goniometer. Once cleaned of drilling fluids, samples for whole-rock and clay fraction analyses were disaggregated using a mortar and pestle. Approximately 5 g of each sample was mixed with isopropyl alcohol and pulverized using a McCrone micronizing mill (Eberl, 2003). The resultant powders were dried, disaggregated, and packed into aluminum sample holders to produce random whole-rock mounts. A separate split of each sample was dispersed in dilute sodium phosphate solution using a sonic probe. Clay-sized (<4 μm) particle fractions were obtained by centrifugation and vacuum deposition of the remaining suspensions onto silver membrane filters to produce oriented clay mineral aggregates. Membrane mounts were attached to stainless steel slugs and exposed to ethylene glycol vapor for a minimum of 24 hr.

Thin sections from 15 selected core samples were examined using a Leica DM 1B02 petrographic microscope, and the images were captured using an integrated digital camera (Leica DFC320). Nine of them, representing different lithofacies, were milled by an Ar ion beam and studied using high-resolution field emission scanning electron microscopy (SEM) to observe micro- and nanosized pores (Loucks et al., 2009). To investigate the mineralogy and texture of the samples, SEM imaging with both secondary electron and backscattered electron (BSE) modes with a FEI Quanta 450 was used. The BSE mode allows mineral phases to be differentiated according to atomic number. For selected areas, a Carl Zeiss Sigma 500 equipped with an electron probe microanalyzer (EPMA; JEOL JXA-8230) was used to create in situ mineral maps based on element distribution. For x-ray computed tomography (CT) scanning, two samples of different rock fabrics were cut into small plugs (2 × 10 mm), and micropores were observed using a General Electric Company phoenix nanotom S. Three-dimensional reconstruction of the images generated was completed using reconstruction software, and identification and calculation of porosity was performed using threshold technology (Lenoir et al., 2007).

Selection and Definition of Lithofacies Parameters

The term lithofacies refers to the rock or association of rocks formed in a certain sedimentary depositional environment. It is the basic unit of shale reservoirs, and a full description of shale lithofacies describes the mineralogy, geochemistry, and hydrocarbon potential of shales (e.g., Slatt and Rodriguez, 2012; Li et al., 2017b). A large number of studies have resulted in a large number of classifications of shale lithofacies (Loucks and Ruppel, 2007; Tang et al., 2016; Li et al., 2017a). Most of these studies used the organic matter content, bedding, and mineral composition as the main components in the definition of shale lithofacies. Combinations of these three factors are used to describe the main petrological characteristics of the shale lithofacies, and this then is indicative of a certain sedimentary depositional environment.

The *TOC* of a shale lithofacies is the most important factor indicating generation potential and storage capacity for shale gas and oil (Jarvie et al., 2007). The Qingshankou shale contains mainly type II1 kerogen and is characterized by relatively high *TOC* (>1 wt. %) when compared with the nonprospective mudstones of the underlying Quantou Formation (Figure 4; Xi et al., 2015). This is consistent with the threshold *TOC* value of 1 wt. % that

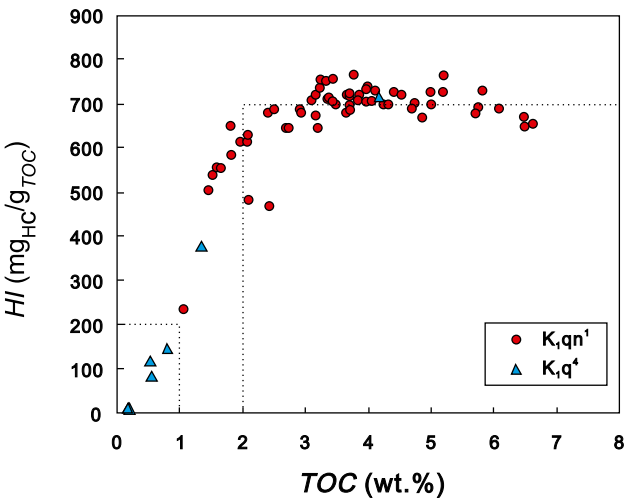

Figure 4. The total organic carbon (*TOC*) versus the hydrogen index (*HI*) of the immature Qingshankou Formation shales in one borehole (data from F. Wang et al., 2016). HC = hydrocarbon; K_1qn^1 = the first member of the Qingshankou Formation; K_1q^4 = the fourth member of Quantou Formation.

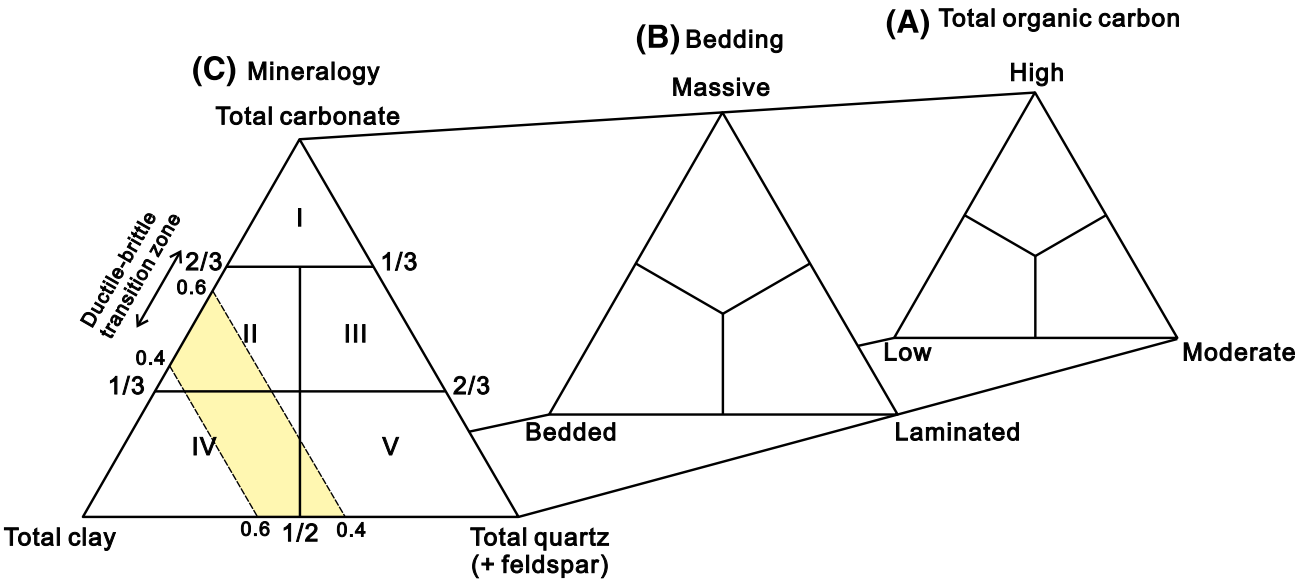

Figure 5. Classification of organic mudstones lithofacies using content of total organic carbon (rich, more than 2 wt. %; moderate, 1–2 wt. %; low, less than 1 wt. % [according to Allix et al., 2010; Anderson, 2014]) (A), bedding types (B), and mineral composition (C). I = calcareous mudstone; II = argillaceous marlstone; III = siliceous marlstone; IV = argillaceous mudstone (shale); V = siliceous mudstone.

must be met for type II1 kerogen–bearing shale lithofacies to be considered as effective source rocks (Bissada, 1982; Katz, 2001; Chen et al., 2011). The plot of *HI* versus *TOC* for immature Qingshankou shales yields a maximum constant *HI* value of 700 mg_{HC}/g_{TOC} (HC = hydrocarbon) from shale lithofacies with *TOC* above 2 wt. %, thus indicating that shale with *TOC* more than 2 wt. % has excellent hydrocarbon generation potential (Figure 4; Schmoker, 1981; Peters and Cassa, 1994; Liu et al., 2014b; F. Wang et al., 2016). In addition, Jarvie et al. (2007) suggest that shale with *TOC* more than 2 wt. % passing through the hydrocarbon generation window results in a high degree of gas adsorption. Taking the *TOC* values of 1 wt. % and 2 wt. % as delimiters, shales can be subdivided into three types: organic-poor shales (*TOC* < 1 wt. %), organic-fair shales (1 wt. % < *TOC* < 2 wt. %), and organic-rich shales (*TOC* > 2 wt. %; Figure 5A).

Fine-grained sedimentary rocks (dominated by grains <62.5 μm) may simultaneously act as hydrocarbon source, reservoir, and sealing rocks. They are normally described as either bedded, laminated, or massive (Lazar et al., 2015). Bedding is a key characteristic of sedimentary rocks that records variations in sediment input and accumulation and benthic energy as well as bioturbation effects. Following the usage of Campbell (1967), a lamina is the smallest megascopic layer in a sedimentary succession that does not show internal layers (commonly fractions of a millimeter to millimeters in thickness). In recent shale studies, lamination is typically interpreted to indicate sedimentation via suspension settling in relatively still and mostly stratified anoxic bottom water, with seasonally controlled intermittent pulses of hydroenergy or anoxia (or both) (e.g., Tyson et al. 1979; Demaison and Moore 1980; Liu et al., 2015). A bed is a relatively conformable succession of genetically related silt laminae or laminasets bounded at the top and base by bedding surfaces related to erosion, nondeposition, or a correlative conformity (commonly centimeters to tens of centimeters in thickness). Not all sedimentary rocks exhibit internal sedimentary features, such as in the case of rapid accumulation of sediments without sedimentary differentiation or sediments that have been aggressively bioturbated. Internal layering can also be hard to distinguish when the texture and composition of a bed varies within a very small range. In this study, we apply the term "massive" to describe beds with these characteristics. This permits categorization of shales by bedding thickness into three types: massive shales (>50 cm), bedded shales (>1 cm), and laminated shales (<10 mm) (Figure 5B).

Mineral composition is also an important factor affecting the petrophysical properties of shale reservoirs: storage capacity, flow capacity, and hydraulic

fracturing effectiveness (Li et al., 2017a). The first composition-based classification scheme for organic mudstones was widely used in the study of gas- and oil-bearing shales in North America by considering the mineralogically controlled shale ductile–brittle transition zone, (Allix et al., 2010; Gamero-Diaz et al., 2013; Anderson, 2014). Figure 5C shows five mudstone types (calcareous or dolomitic mudstones, argillaceous marlstones, siliceous marlstones, argillaceous mudstones, and siliceous mudstones) and their related ductile–brittle transition zones as clay mineral content ranges from 40 to 60 wt. %. When clay mineral content is more than 60 wt. %, shales deform in a ductile manner. By contrast, shales with a clay content of less than 40 wt. % present a brittle response to stress. This makes them favorable candidates for hydraulic fracturing (Rickman et al., 2008).

Types of Shale Lithofacies

As shown in Figure 5, 3 ternary diagrams with 3 shale types categorized by *TOC* and the bedding scale and 5 types of mudstones defined by mineral composition give a possible total of 45 classes of shale lithofacies. The defining characteristics and interrelationships among the shale lithofacies in this study should be considered as arising from climatically induced heterogeneities in a continuous sedimentary system, which naturally occur within certain ranges (Katz and Lin, 2014). Thus, the final number of shale lithofacies classifications will in reality be well below 45.

RESULTS

Bulk Geochemical Parameters

Bulk geochemical parameters of the 42 samples from the first member of the Qingshankou Formation are listed in Table 1. The *TOC* ranges from 0.12 to 3.62 wt. %, with an average value of 1.18 wt. %. The S_1 values range from 0 to 4.5 mg_{HC}/g_{rock}, with an average value of 1.1 mg_{HC}/g_{rock}. The samples give pyrolysis S_2 yield values in the range of 0.1 to 14.9 mg_{HC}/g_{rock}, with an average value of 3.5 mg_{HC}/g_{rock}. The *HI* values range from 57 to 582 mg_{HC}/g_{TOC} (average value 253 mg_{HC}/g_{TOC}). Plotting these results on an *HI* versus T_{max} diagram (Figure 6A; Espitalié et al., 1984) shows that the sample points are widely distributed within the regions characteristic of kerogen types II and III. Plotting S_2 versus *TOC* (Figure 6B; Langford and Blanc-Valleron, 1990) results in an average "true" *HI* of approximately 396 mg_{HC}/g_{TOC} from the slope of the linear regression line (coefficient of determination $[R^2] = 0.87$). These data indicate a high degree of organic type heterogeneity within the shale lithofacies samples, this heterogeneity being especially evident when the sample *TOC* is less than 2 wt. %. The T_{max} values range from 410°C to 459°C (average value 439°C). Samples with lower calculated T_{max} values have correspondingly lower *TOC* (Figure 6C) and reflect occurrences of migrated hydrocarbons into nonsource shale lithofacies with *TOC* less than 1 wt. %, such as siltstones or intercalated limestones. If the T_{max} values of these samples are excluded, the samples with *TOC* ranging from 1 to 2 wt. % have a more uniform *HI* value (Figure 6B). Furthermore, T_{max} values are in the range of 435°C–460°C, with the median of the distribution interval being approximately 450°C (Figure 6C), indicating that the organic matter in most of the samples is within the hydrocarbon generation window.

When geochemistry of these shale lithofacies samples is compared with the geochemical characteristics of immature shales (Figure 4), the decrease in *HI* values from 700 to 396 mg_{HC}/g_{TOC} and variations between kerogen types II1 and II2, which indicate the degree of thermal evolution of the organic matter within shales, both indicate that hydrocarbons have been generated in these source-rock samples.

Mineralogy and Lithology

Mineralogically, the first shale member of the Qingshankou Formation is composed of quartz (3.2–47.1 wt. %; average 31.9 wt. %), plagioclase (4.1–71.5 wt. %; average 30.4 wt. %), and clay (0–52.0 wt. %; average 16.9 wt. %), followed by calcite (0–60.2 wt. %; average 8.8 wt. %), dolomite (0–59.2 wt. %; average 6.5 wt. %), K-feldspar (0–15.5 wt. %; average 3.2 wt. %), and pyrite (0–9.3 wt. %; average 1.8 wt. %).

Combining the results from the SEM and EPMA investigations with the mineral compositions revealed by XRD methods (Figure 7A), the composition of the silt and clay particles is seen to be dominated by K, Si, Ca, and Fe. Clay minerals are hard to distinguish because of their tiny particle size. Pyrite and siderite

Table 1. Bulk Geochemical Parameters and X-Ray Diffraction Results of the Samples from the First Member of the Qingshankou Formation

		Rock-Eval						Whole-Rock Mineralogy, wt. %								Clay (Phyllosilicate) Mineralogy, wt. %			
Lithofacies	Depth, m (ft)	*TOC*, wt. %	T_{max}, °C	S_1, mg_{HC}/g	S_2, mg_{HC}/g	S_3, mg_{CO_2}/g	*HI*, mg_{HC}/g_{TOC}	Quartz	K-feldspar	Plagioclase	Calcite	(Fe-) Dolomite	Siderite	Pyrite	Total Clay	Illite	Chlorite	Illite/ Smectite	Illite/ Chlorite
HMSM	2358.15 (7736.71)	2.01	439	1.7	5.4	0.1	266	28.5	3.8	33.5	0.0	0.5	6.8	0.0	26.9	95	0	5	0
	2109.20 (6919.95)	3.62	453	3.2	13.5	0.1	372	39.7	1.3	21.0	0.0	9.3	0.0	0.0	28.7	77	13	10	0
	2142.28 (7028.48)	2.65	452	1.0	10.2	0.2	385	29.9	2.2	27.0	0.0	1.2	0.0	9.3	30.4	79	10	11	0
	2267.06 (7437.86)	2.76	447	3.3	8.1	0.2	293	32.8	1.8	22.3	3.4	1.4	1.6	2.0	34.6	74	13	13	0
	2318.73 (7607.38)	2.00	434	0.7	5.9	0.2	294	33.9	1.9	20.8	1.9	0.0	1.9	3.9	35.7	71	14	15	0
	2094.15 (6870.57)	3.25	450	3.2	14.9	0.2	460	34.0	0.0	21.1	4.3	0.0	0.0	3.8	36.7	55	24	21	0
	2098.33 (6884.28)	3.34	449	4.5	13.8	0.3	413	37.9	0.0	7.7	0.0	0.0	0.0	2.4	52.0	69	13	15	3
MMSM	2186.70 (7174.21)	0.96	441	0.8	2.1	0.2	222	36.2	2.4	21.4	4.7	0.0	0.0	3.0	32.3	77	11	12	0
	2175.23 (7136.58)	1.90	439	2.2	5.8	0.2	302	42.6	2.5	21.4	0.0	0.0	1.8	2.8	29.0	83	7	10	0
	1980.65 (6498.20)	1.62	449	1.0	7.4	0.1	460	31.5	4.2	19.9	0.9	0.0	0.0	8.6	35.0	83	5	12	0
	1957.40 (6421.92)	1.46	446	0.5	6.2	0.3	425	33.2	0.0	24.6	1.9	0.0	1.6	2.7	36.0	73	14	13	0
MLSM	2317.11 (7602.07)	1.00	443	0.9	1.8	0.1	176	35.3	4.8	47.7	0.0	3.7	0.0	3.1	5.4	95	0	5	0
	1977.94 (6489.30)	1.27	439	2.6	4.4	0.1	350	38.6	2.4	40.0	3.1	1.5	0.0	2.3	12.1	70	16	14	0
	2361.95 (7749.18)	1.54	459	0.5	1.2	0.1	79	41.8	2.6	40.9	0.4	0.9	0.0	0.0	13.3	89	0	11	0
	2205.81 (7236.91)	1.04	453	0.3	0.8	0.1	75	33.7	3.6	44.1	1.1	0.0	0.0	2.0	15.4	78	9	13	0
	2321.86 (7617.65)	1.39	446	0.8	1.2	0.1	89	25.4	10.2	37.3	0.0	4.4	3.2	3.9	15.6	90	0	10	0
	2170.73 (7121.82)	1.40	445	1.7	2.9	0.1	204	39.2	4.4	39.1	0.0	0.0	0.0	0.0	17.3	73	15	12	0
	2365.32 (7760.24)	1.90	435	3.8	5.0	0.1	260	39.4	0.0	37.1	0.4	0.0	0.0	0.0	23.1	54	25	11	10
	2202.31 (7225.43)	1.00	449	0.5	2.3	0.1	231	37.2	3.5	28.4	4.0	0.0	0.0	2.1	24.7	81	7	12	0
	2139.33 (7018.80)	1.38	448	0.3	3.3	0.2	238	38.8	4.6	31.4	0.0	0.4	0.0	0.0	24.8	82	8	10	0
LLSM	2343.17 (7687.57)	0.56	448	0.3	0.5	0.2	89	21.5	5.9	65.3	0.0	6.5	0.8	0.0	0.0	91	0	9	0
	2320.66 (7613.71)	0.65	437	0.5	1.2	0.2	177	28.3	1.6	40.5	10.8	11.3	0.0	5.1	2.4	71	0	29	0
	2354.92 (7726.12)	0.67	412	0.9	1.3	0.2	188	18.7	1.6	27.3	38.4	7.9	0.0	1.2	4.9	20	37	18	25
	2184.38 (7166.60)	0.68	445	0.5	1.1	0.1	156	31.2	2.9	19.4	0.0	22.3	0.0	3.8	20.4	76	11	13	0
	1881.56 (6173.10)	0.92	444	0.2	2.4	0.2	259	32.8	2.3	21.5	8.0	9.3	0.0	4.2	21.9	80	9	11	0
	2336.32 (7665.09)	1.21	410	1.5	3.2	0.1	264	31.4	5.0	30.0	17.1	2.6	0.0	0.0	13.9	73	15	12	0
	2260.36 (7415.88)	0.58	424	0.5	1.4	0.1	247	28.2	4.5	34.3	19.8	4.7	0.0	0.0	8.4	65	24	11	0
	1950.75 (6400.10)	0.68	442	0.3	1.4	0.1	199	40.6	10.3	36.5	1.1	0.0	0.0	1.8	9.8	52	32	16	0
	1979.55 (6494.59)	0.74	446	0.3	1.5	0.2	202	38.3	4.7	23.8	0.9	0.0	0.0	0.0	32.3	84	9	7	0

(*continued*)

Table 1. Continued

		Rock-Eval						Whole-Rock Mineralogy, wt. %								Clay (Phyllosilicate) Mineralogy, wt. %			
Lithofacies	Depth, m (ft)	*TOC*, wt. %	T_{max}, °C	S_1, mg_{HC}/g	S_2, mg_{HC}/g	S_3, mg_{CO_2}/g	*HI*, mg_{HC}/g_{TOC}	Quartz	K-feldspar	Plagioclase	Calcite	(Fe-) Dolomite	Siderite	Pyrite	Total Clay	Illite	Chlorite	Illite/ Smectite	Illite/ Chlorite
LBCM	2321.61 (7616.83)	0.44	420	0.5	0.8	0.2	171	3.2	0.0	8.2	29.3	59.2	0.0	0.0	0.0	63	0	37	0
	2341.08 (7680.71)	0.33	424	0.9	0.9	0.2	262	6.2	0.0	5.0	50.4	38.4	0.0	0.0	0.0	0	0	0	0
	2096.27 (6877.53)	0.48	430	0.9	1.6	0.2	325	4.8	0.0	5.1	60.0	28.8	0.0	0.0	1.4	47	37	16	0
	2087.73 (6849.51)	0.57	428	2.1	3.3	0.2	582	8.4	0.0	4.1	30.7	49.9	0.0	0.0	6.8	47	35	18	0
LBSS	2332.07 (7651.15)	0.12	425	0.1	0.1	0.1	57	23.4	4.2	71.5	0.0	0.0	0.0	0.9	0.0	0	0	0	0
	2036.89 (6682.71)	0.54	426	1.9	2.3	0.2	430	15.6	0.0	11.8	60.2	7.9	0.0	1.4	3.1	45	35	20	0
	2187.38 (7176.44)	0.46	433	1.9	2.7	0.0	571	43.8	1.9	42.6	5.6	0.0	0.0	2.9	3.3	65	23	12	0
	1981.15 (6499.84)	0.18	433	0.0	0.3	0.1	152	42.4	2.9	48.9	0.0	0.8	0.0	1.1	4.1	82	0	18	0
	2192.10 (7191.93)	0.29	437	0.1	0.2	0.1	82	45.8	2.3	39.7	6.0	0.0	0.0	0.9	5.5	81	0	19	0
	2138.83 (7017.16)	0.66	445	0.4	0.7	0.2	106	35.3	15.5	41.7	0.0	0.5	0.0	0.0	6.9	47	38	6	9
	2311.83 (7584.74)	0.85	428	0.7	2.2	0.1	254	47.1	0.0	40.5	2.3	0.0	0.0	0.0	10.1	46	35	10	9
	2157.96 (7079.92)	0.24	435	0.2	0.4	0.1	157	37.9	6.0	40.6	2.7	0.0	0.0	2.3	10.4	79	10	11	0
	2270.56 (7449.34)	0.35	438	0.1	0.3	0.1	91	44.4	7.1	32.7	0.2	0.0	0.0	0.0	15.7	77	14	9	0

Abbreviations: HC = hydrocarbon; *HI* = hydrogen index; HMSM = high-*TOC* massive siliceous mudstone; LBCM = low-*TOC* bedded calcareous mudstone; LBSS = low-*TOC* bedded siliceous siltstone; LLSM = low-*TOC* laminated siliceous mudstone; MLSM = moderate-*TOC* laminated siliceous mudstone; MMSM = moderate-*TOC* massive siliceous mudstone; S_1 = the amount of free hydrocarbon in the sample; S_2 = the amount of pyrolyzate released from kerogen; S_3 = amount of CO_2 produced during pyrolysis; T_{max} = the temperature of maximum hydrocarbon generation; *TOC* = total organic carbon.

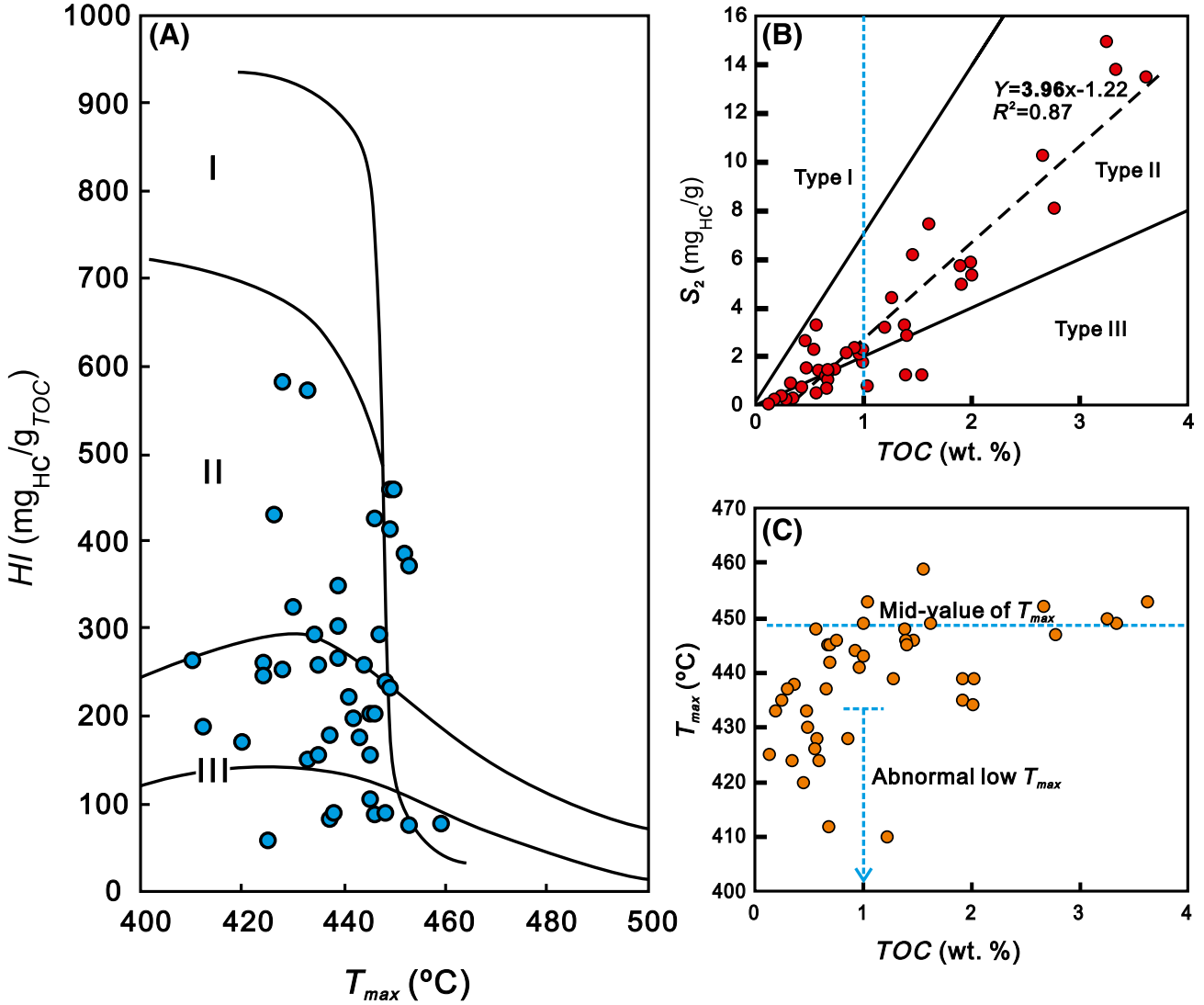

Figure 6. (A) Plot of the temperature of maximum hydrocarbon generation (T_{max}) versus hydrogen index (*HI*) (according to Espitalié et al. [1984]) outlining kerogen types and maturity of sedimentary rocks from the first member of the Qingshankou Formation. (B) Correlations between total organic carbon (*TOC*) and the amount of pyrolyzate released from kerogen (S_2) [according to Langford and Blanc-Valleron (1990)]. (C) Plot of T_{max} and *TOC*. HC = hydrocarbon; R^2 = coefficient of determination.

with a range of grain-size distributions are dispersed within the shale matrix. The laminated samples show obvious grain-size changes where silt and clay laminae terminate sharply at their margins. The lamination is generally continuous, planar, and parallel in hand specimens, but discontinuous, wavy laminae and ripple cross-laminae are documented by microscopic observations. The silt laminae mainly consist of rounded quartz and feldspar grains, showing hard cementation by calcitic minerals (e.g., calcite). The clay laminae have more clusters of pyrite framboids (Figure 7B). Ostracod limestone exhibits much higher calcite content and has very obvious cyclic sequences distinguished by different Ca abundance (Figure 7C). Pyrite occurs between calcareous shells in these samples. None of the samples display any evidence of bioturbation, indicating a stratified water column with anoxic, highly saline bottom water (Ma et al., 2016).

A mineralogical constituent ternary diagram for the first shale member of the Qingshankou Formation shows the relative proportions of total clay, total carbonate, and other minerals (i.e., quartz and feldspars; Figure 8). Most samples plot inside the region classified as siliceous mudstone, showing high whole-rock quartz and feldspar content. This was confirmed by the EPMA scanning maps for selected elements.

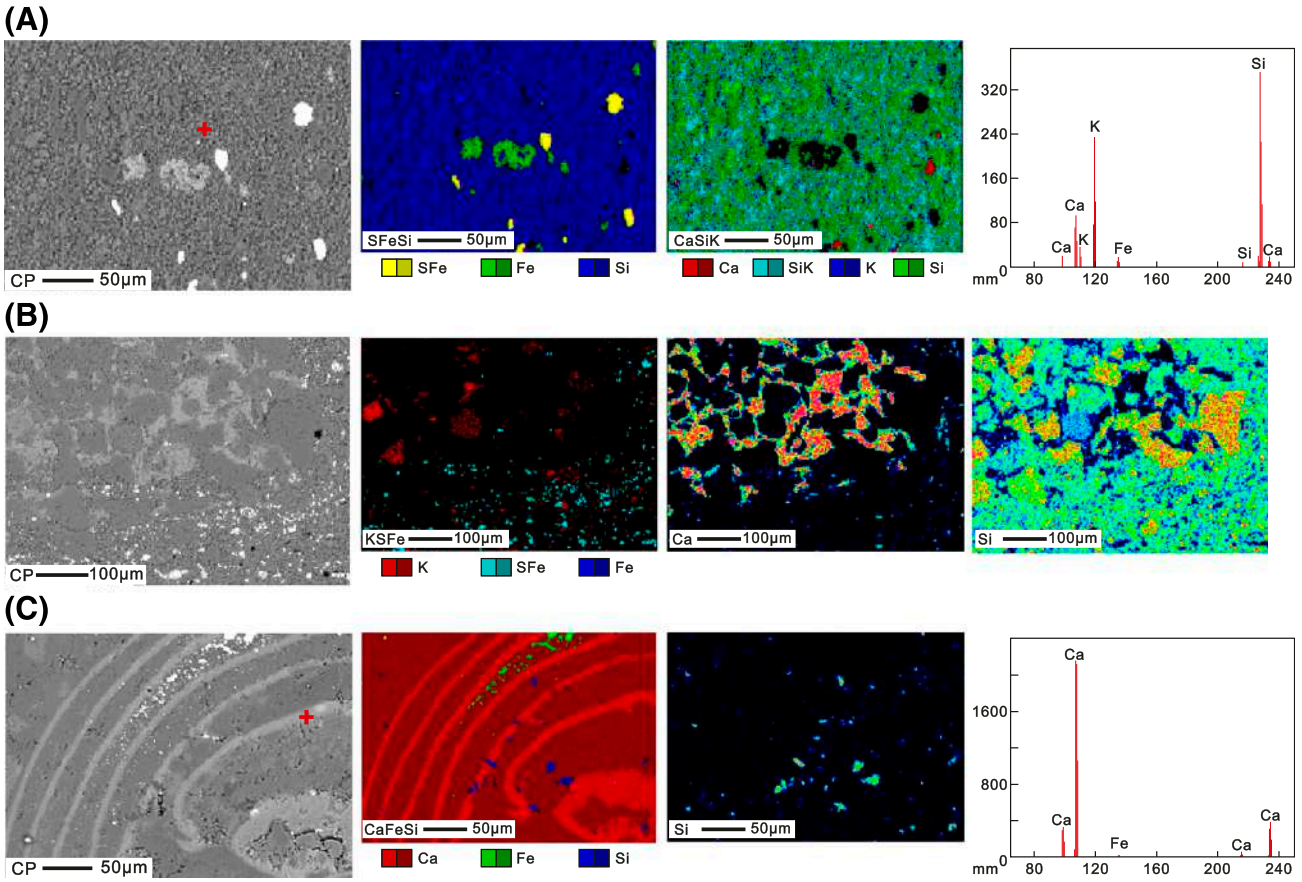

Figure 7. Typical mineral composition features of the Qingshankou Formation shales in the Songliao Basin. Grayscale figures are the scanning electron microscope photos, with the red cross showing the position of electron probe microanalysis. Color figures are the scanning maps of selected elements. These figures show abundance of quartz and feldspar with scattered pyrites and siderites (A), calcite cementation intercoarse particles such as quartz and feldspar (B), as well as scattered pyrites within fine-grained matrix, and the shell structure of the ostracod distinguished by different calcite contents (C). CP = composition.

As shown in Figure 8A, we colored the samples according to their *TOC* and bedding thickness. This makes it straightforward to show that increasing sample clay content is associated with increasing *TOC* and a change in bedding style from bedded or laminated to massive (Figure 8B). Some laminated samples showed high carbonate content and plotted in the region of siliceous marlstones and the upper part of siliceous mudstones, indicating the occurrence of intergranular calcic cements (Figure 7B). The bedded samples plotted either near the 100% carbonate end of the ternary diagram or the 100% quartz and feldspar end (Figure 8). Combining this observation with the results of the core analysis and EPMA under SEM allowed these two suites of bedded samples to be classified as calcareous mudstones (containing calcic ostracods; Figure 7C) and interbedded siltstones, respectively.

Lithofacies

A combination of detailed core descriptions, microscopic observations, and mineralogical and geochemical analyses allowed the determination of the *TOC*, fabric, and mineral composition of 42 samples from 11 wells, which led to the recognition of a total of 7 lithofacies types in the Qingshankou shale in the northern Songliao Basin (Figure 9; Table 1). These include high-*TOC* laminated argillaceous mudstones (HLAM), high-*TOC* massive siliceous mudstones (HMSM), moderate-*TOC* massive siliceous mudstones (MMSM), moderate-*TOC* laminated siliceous mudstones (MLSM), low-*TOC* laminated siliceous mudstones (LLSM), low-*TOC* bedded siliceous siltstones (LBSS), and low-*TOC* bedded calcareous mudstones (LBCM).

The HLAM (dark brown to black in color) showed opening foliations containing bitumen, exhibiting

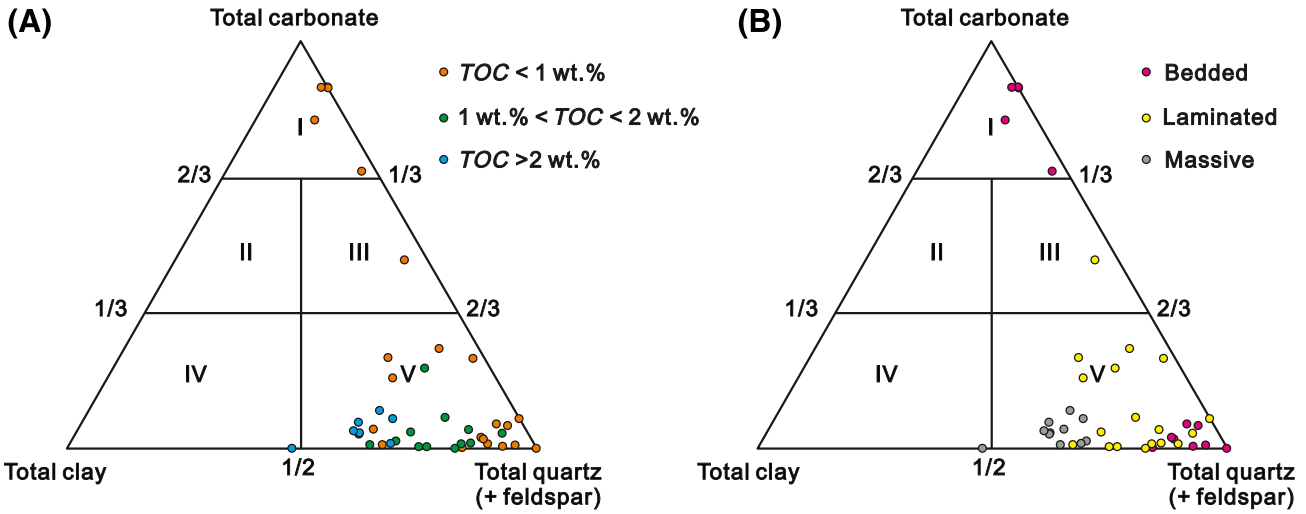

Figure 8. Ternary diagram showing mineral composition and total organic carbon (*TOC*) (A), and mineral composition and rock fabric (B) of the Qingshankou Formation shale in the northern Songliao Basin. I = calcareous mudstone; II = argillaceous marlstone; III = siliceous marlstone; IV = argillaceous mudstone (shale); V = siliceous mudstone.

a continuous fabric that consists of parallel clay minerals and organic matter particles (Figure 9A). The HLAM have the same petrological and geochemical characteristics as the "oil shale" identified by Jia et al. (2013b), which yields substantial amounts of oil that can be developed by open-cast or conventional underground mining at or near the surface in the southern part of the Songliao Basin (Dyni, 2003). Both HMSM and MMSM show homogeneous textures and a dark gray to black color depending on the *TOC* (Figure 9B, C). A similar fabric is found in MLSM and LLSM, which occur as laminasets that consist of an interbedded dark clay lamina with organic matter particles and light-colored silt laminae. The density and thickness of the organic-rich clay laminae control the color and the *TOC* of the samples (Figure 9D, E). Most LBSS also show blocky and homogeneous textures, with only small regions showing isolated, continuous to discontinuous wavy clay-laminae (Figure 9F). The LBCM are dark-colored and could be called an ostracod limestone characterized by the presence of silt-sized ostracods and minor occurrences of black clay laminae (Figure 9G). Under a microscope, the sparry calcic ostracod grains, which are commonly strongly recrystallized, mix with aphanitic grains.

Scatter plots show a modest correlation between total clay content and *TOC* (Figure 10A; $R^2 = 0.62$). With the lack of both inorganic dilution by coarse-grained sediments and fabric formed under intense dynamic conditions, this relationship is a product of slow sedimentary rates and suspension within a standing water column (i.e., hemideep to deep lake conditions; Liu et al., 2015). Relatively high average clay-mineral content and *TOC* are found in HMSM lithofacies, which are 35.5 wt. % and 2.8 wt. % less than the values seen in the HLAM samples (60.0 wt. % and 5 wt. %), respectively (Figure 10B; Jia et al., 2013a). As *TOC* and total clay content decrease together, this results in the sequential lithofacies change from HLAM, HMSM, MMSM, MLSM, and LLSM to LBCM and LBSS (Figure 10).

Spatial Distribution of Lithofacies

The spatial distribution of the first member of the Qingshankou Formation shales in the northern Songliao Basin was studied on the basis of high-resolution mineralogical and bulk geochemical data from cores, well logs, and wavelet depth–frequency analysis (wavelet methods from Wu et al., 2013). Maximum lake extent occurred during the deposition of the first member of the Qingshankou Formation. From bottom to top, the Qingshankou Formation demonstrates a progressive–regressive sedimentary sequence with decreasing water-column height (Zhu et al., 2017). As shown in Figure 11, HMSM and MLSM facies are the predominant lithofacies, and the evidence for the progressive shallowing of the lacustrine

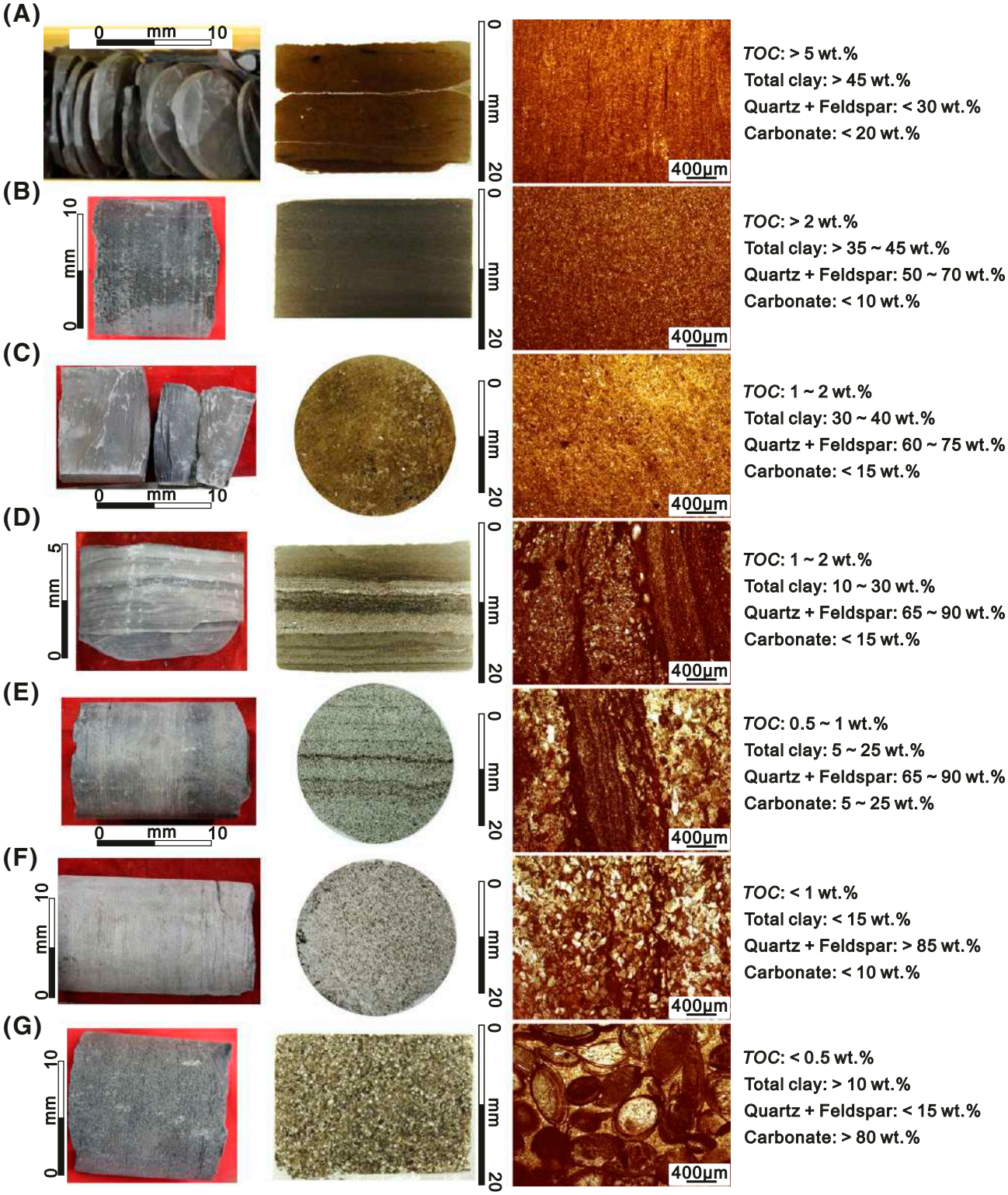

Figure 9. Lithofacies within the Qingshankou shale. Core image, thin section image, and transmitted light image show example of each individual facies. (A) High–total organic carbon (*TOC*) laminated argillaceous mudstone. (B) High-*TOC* massive siliceous mudstone. (C) Moderate-*TOC* massive siliceous mudstone. (D) Moderate-*TOC* laminated siliceous mudstone. (E) Low-*TOC* laminated siliceous mudstone. (F) Low-*TOC* bedded siliceous siltstone. (G) Low-*TOC* bedded calcareous mudstone. Each lithofacies description includes a range of *TOC*, total clay, quartz + feldspar, and carbonate.

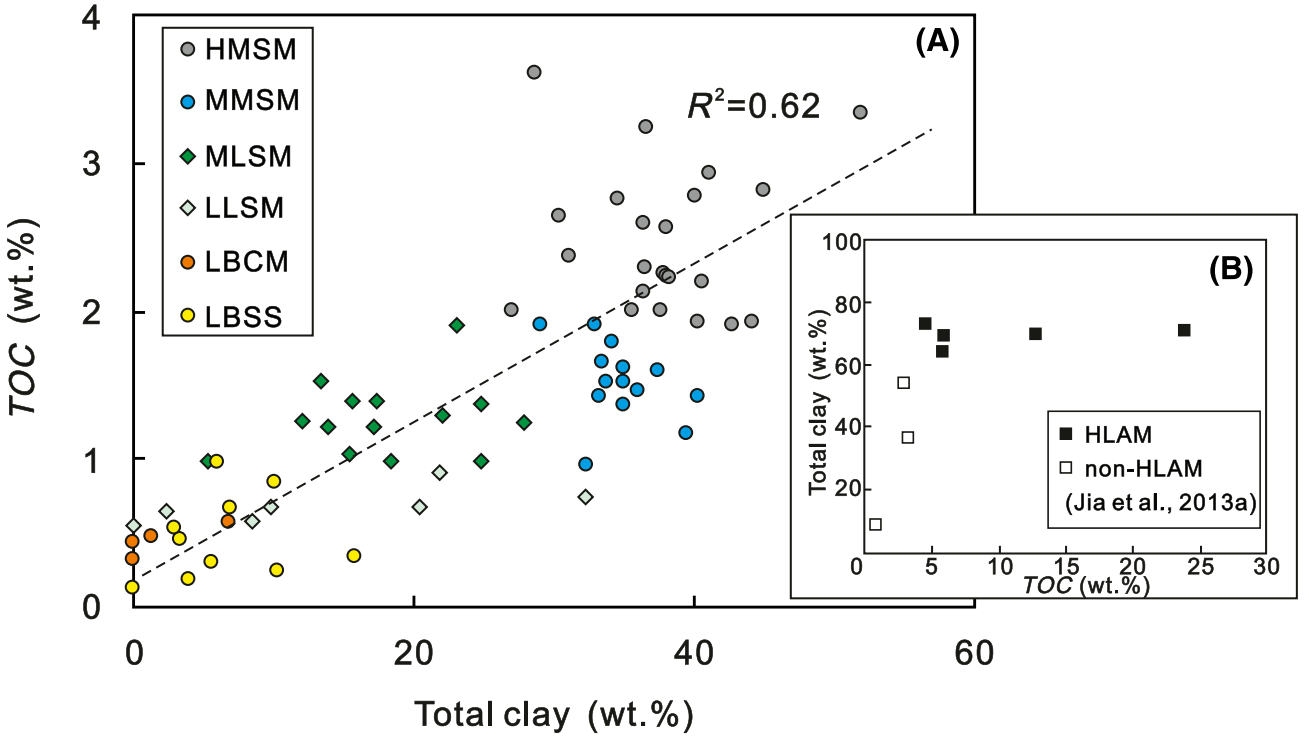

Figure 10. Total organic carbon (*TOC*) versus total clay contents of first member of the Qingshankou Formation. (A) This study. (B) High-*TOC* laminated argillaceous mudstone (HLAM) oil shale data from Jia et al., 2013a. HMSM = high-*TOC* massive siliceous mudstone; LBCM = low-*TOC* bedded calcareous mudstone; LBSS = low-*TOC* bedded siliceous siltstone; LLSM = low-*TOC* laminated siliceous mudstone; MLSM = moderate-*TOC* laminated siliceous mudstone; MMSM = moderate-*TOC* massive siliceous mudstone; R^2 = coefficient of determination.

system is seen from the vertical variations in shale lithofacies, a generally decreasing frequency of occurrence of HMSM and pyrite content, as well as increasing frequency of occurrence of LBCM. The occurrence of pyrite together with calcic minerals indicates a shallow saline water column (Liu et al., 2018). The sedimentary section could be further subdivided into three short-term cycles (from SSC1 to SSC3), each containing a complete transgressive–regressive system tract. The bottom interface of the Qingshankou Formation is a sharp lithologic contact, above which occur dark mudstones deposited in a hemideep to deep lake environment. The *TOC* increases upward at first and then decreases, with shale lithofacies gradually evolving from LBSS, LBCM, or LLSM at the lower or upper section of each cycle to HMSM in the middle of the section. Various types of shale lithofacies are present at the ends of short-term cycles, which represent periods of relatively high depositional heterogeneity.

A northeast–southwest cross section parallel to the direction of sediment input (i.e., from delta to deep lake facies) shows the influence on sediment mineralogy of silt grains that originate from the shallow-water delta (LBSS facies) (Zhu et al., 2017) (Figure 12). The LBSS changes to LLSM, MLSM, MMSM, and HMSM laterally with increasing clay content and *TOC*. This section also illustrates that MLSM, MMSM, and HMSM facies have a high lateral depositional continuity in the semideep to deep lake environment.

As discussed above, study of the spatial distribution of lithofacies in the first member of the Qingshankou Formation shows that vertical lithological variations were controlled by the transgressive or regressive sequences in the short-term cycles and that lateral variations were controlled by the input of terrigenous material.

DISCUSSION

Depositional Setting and Processes

During the deposition of the Qingshankou Formation, the Songliao Basin underwent large-scale lake

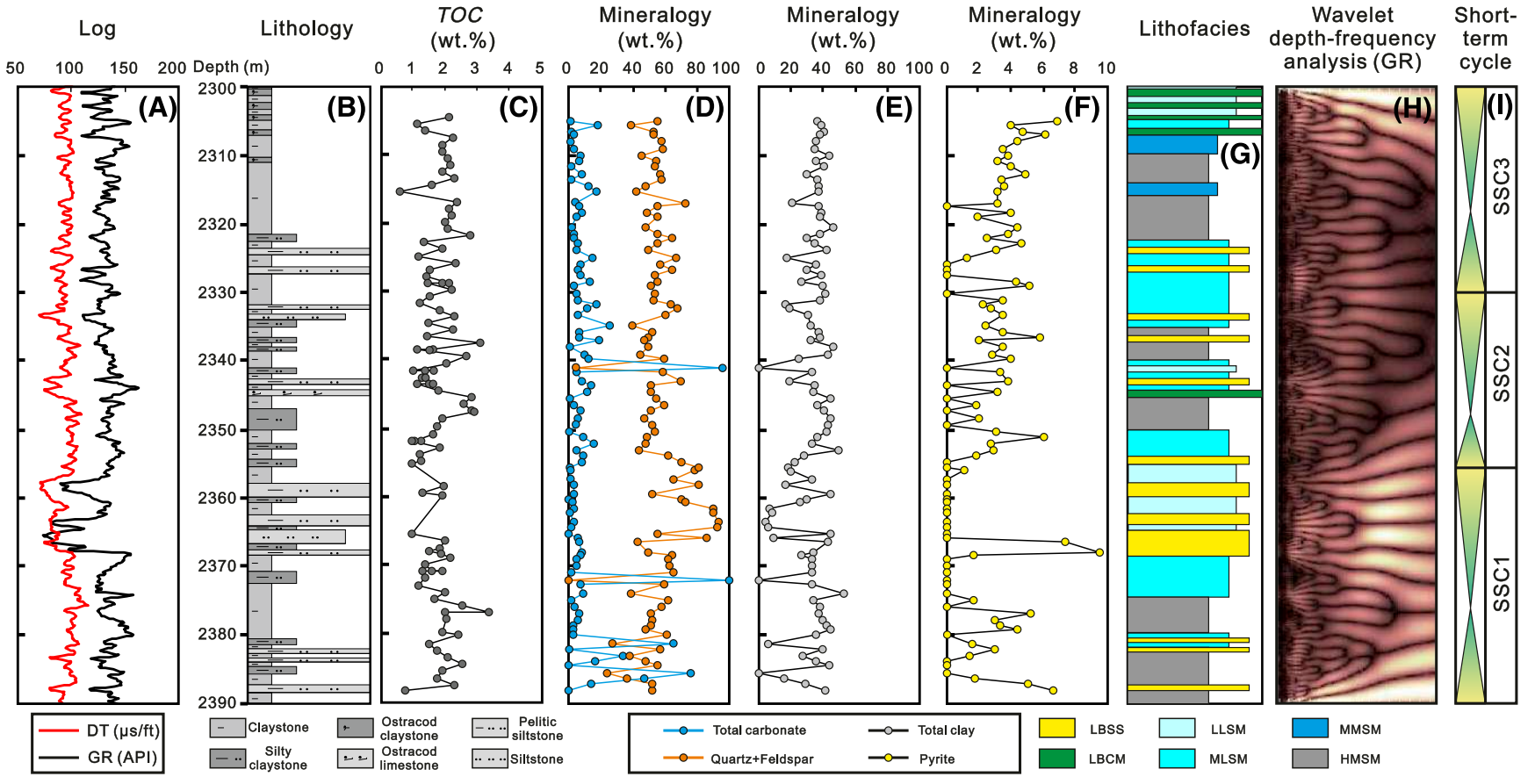

Figure 11. Characteristics of shale lithofacies and short-term sedimentary cycles of the first member of the Qingshankou Formation from a borehole in the Gulong sag, Songliao Basin: (A) logs; (B) lithological profile; (C) total organic carbon (*TOC*); (D–F) mineral composition; (G) lithofacies profile; (H) wavelet depth–frequency; (I) short-term cycle. DT = sonic interval transit time; GR = natural gamma ray; HMSM = high-*TOC* massive siliceous mudstone; LBCM = low-*TOC* bedded calcareous mudstone; LBSS = low-*TOC* bedded siliceous siltstone; LLSM = low-*TOC* laminated siliceous mudstone; MLSM = moderate-*TOC* laminated siliceous mudstone; MMSM = moderate-*TOC* massive siliceous mudstone; SSC = short-term cycle.

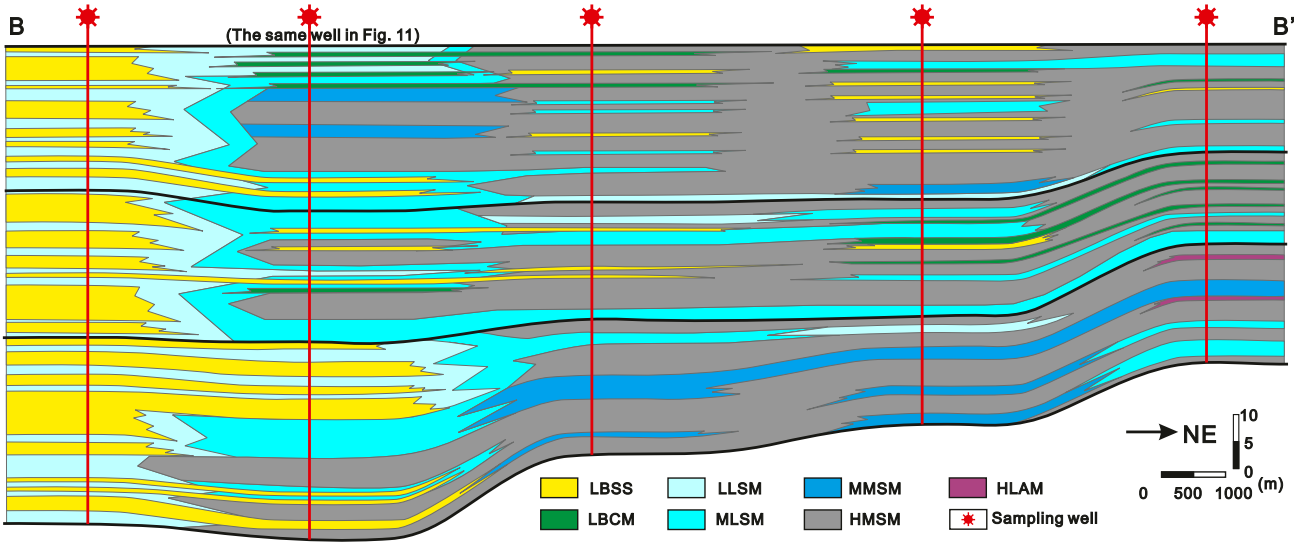

Figure 12. Northeast–southwest cross section of the first member of the Qingshankou Formation in the northwest Gulong sag, Songliao Basin, showing the correlation of the different lithofacies. The location is shown in Figure 1. HLAM = high–total organic carbon (*TOC*) laminated argillaceous mudstone; HMSM = high-*TOC* massive siliceous mudstone; LBCM = low-*TOC* bedded calcareous mudstone; LBSS = low-*TOC* bedded siliceous siltstone; LLSM = low-*TOC* laminated siliceous mudstone; MLSM = moderate-*TOC* laminated siliceous mudstone; MMSM = moderate-*TOC* massive siliceous mudstone.

transgression as subsidence increased. The climate was hot and humid (Jia et al., 2013b). The Yingtai water system, which developed in the western part of the depression, was deposited on the delta front. It gradually transitions to the east into semideep–deep lacustrine deposits (Li et al., 1994). Affected by factors such as an abundant supply of water from the delta system, the development of lake slope breaks, and rapid lake expansion, the sedimentary rocks at the delta front show repeated evidence for gravity-related collapse along the slope. The semideep–deep lake shales commonly contain lenticular sandstone bodies that originate from mass transport or turbidite flows.

Spatial and temporal lithofacies distribution controlling the shale reservoir quality are defined by a combination of organic geochemical, mineralogical, and petrographic data, which are a response to depositional setting and sedimentation processes. (Ma et al., 2016; Newport et al., 2016). Seven lithofacies, which can be differentiated by *T*OC, bedding, and total clay content, were deposited at different water depths. We developed a preliminary depositional model to interpret the evolution of the depositional environments of the first member of the Qingshankou Formation.

The *T*OC is well correlated with the short-term cycles, suggesting that the accumulation of organic matter in the mudstones was controlled by depositional and water conditions as discussed above. Filling sequences composed of different lithofacies characterized by increasing *T*OC and total clay content and decreasing layer thickness (i.e., from bedded to laminated then to massive sedimentary structures) represents an overall trend from shallow-water to deep-water depositional environments. Where the filling sequence composition is reversed, this represents a depositional environment that transitions from a deep to a shallow lake. The correlation between *T*OC and clay content (Figure 10) relates to the adsorption of organic matter into the clays following algal decomposition during cold seasons, with the sedimentary sequence protected under a stratified water column (e.g., C. Liu et al., 2017). The lack of bioturbation indicates an anoxic water bottom, which also promotes the preservation of organic matter. Thus, HLAM and HMSM, which are the most organic-rich lithofacies, are shown to represent a deep-water subtidal zone with low-energy deposition associated with transgression (Heath et al., 2011).

Generally, a new cycle begins with the deposition of a sand body unconformably on the underlying layers. In a fine-grained sedimentary system, this layer of sandstone and siltstone is thin and discontinuous and interpreted as being the outer front of the delta or

distal bar facies deposited in shallow water. Thus, LBSS formed at the base of a transgressive half-cycle (Figure 13). Following lake-level rise or a decrease in terrigenous input, the thickness of bedded siltstones decreases and clay content increases. The observed laminated texture forms as a result of suspension settling from surface waters or interflows (river input plumes) interlaminated with grains and clasts supplied by turbidites (Gierlowski-Kordesch, 2010). In this case, MLSM formed following the deposition of LLSM in the vertical stratigraphic column. The most widely occurring lithofacies are HMSM and MMSM, indicating the negligible influence of continental runoff during deposition (Schieber and Southard, 2009; Schieber and Yawar, 2009). Continuous planar lamination suggests low-energy deposition conditions (Abouelresh and Slatt, 2012). The lack of wavy lamination and ripple cross-lamination imply an absence of sediment reworking by wave activity (Lazar et al., 2015). Thus, HLAM is interpreted as having been deposited in a moderately deep to deep lacustrine environment during the period of maximum lake level (characterized by very slow sedimentation rates), resulting in the enrichment of organic matter in the sedimentary rocks.

In the regressive system tract, stacking patterns of lithofacies reverse with falling water level. At the end of a short-term cycle, the lake level is shallow, forming LBSS in the case of abundant detrital input or LBCM in the case of limited detrital input into oxygen- and

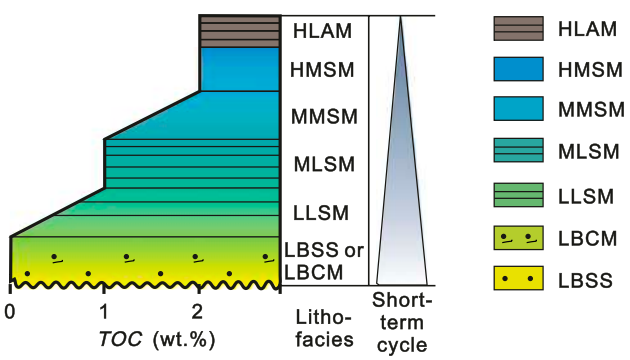

Figure 13. Typical succession of lithofacies within a classic transgressive sequence. HLAM = high–total organic carbon (*TOC*) laminated argillaceous mudstone; HMSM = high-*TOC* massive siliceous mudstone; LBCM = low-*TOC* bedded calcareous mudstone; LBSS = low-*TOC* bedded siliceous siltstone; LLSM = low-*TOC* laminated siliceous mudstone; MLSM = moderate-*TOC* laminated siliceous mudstone; MMSM = moderate-*TOC* massive siliceous mudstone.

nutrition-rich shallow waters in a semihumid to humid climate favorable for an increase in the abundance of ostracods. The homogeneous fabric, uncrushed ostracod fragments, and lack of bioturbation in LBCM reflect the original deposition in a relatively low-energy, poorly oxygenated lacustrine setting (Bruhn, 1999; Ma et al., 2016). Stacking patterns and a sequence stratigraphic framework both demonstrate how sedimentation periodicity is controlled by the short-term cycles. Vertical changes of lithofacies are generally gradual but can be sharp at the bedding surfaces of bedded siltstones.

Hydrocarbon Generation Potential

Shale oil charge within the source rock depends on the volume of hydrocarbons generated and retained. Applying the terminology of Peters and Cassa (1994), *TOC* and Rock-Eval S_2 values show that all the HMSM samples show a good to very good potential for oil generation and emplacement (Figure 14A). The MMSM samples also show a good petroleum generation potential, followed by MLSM and LLSM facies. The LBCM and LBSS samples have a poor potential for petroleum generation.

Geochemical parameters, including the Rock-Eval S_1, *OSI*, and *PI* have been used to predict the presence of mobile oil and provide guidance to shale oil exploration. The plot of S_1 versus *TOC* is considered to be a useful indicator to evaluate whether hydrocarbons are in situ or have migrated (Espitalié et al., 1977; Sonnenberg et al., 2011). As shown in Figure 14B, HMSM and MMSM, MLSM and LLSM, and LBCM and LBSS have different positive S_1 versus *TOC* correlation trends. This may be related to different sedimentary structures within these three lithofacies groups (from blocky to lamellar then to layered).

We found that HMSM, MLSM, LBCM, and LBSS have relatively high S_1 values reaching moderate to high saturations, indicating that these rocks have a higher free hydrocarbon content. Because of the extremely poor hydrocarbon generation potential of LBSS, several samples plot into regions indicating low to zero saturation of indigenous hydrocarbons. This is related to the fair to poor generative potential of these rocks under extremely low-permeability migration conditions.

Plot of pyrolysis T_{max} versus *PI* (Figure 14C) confirm that hydrocarbons in certain LLSM, LBSS, and LBCM samples had migrated into these lithofacies

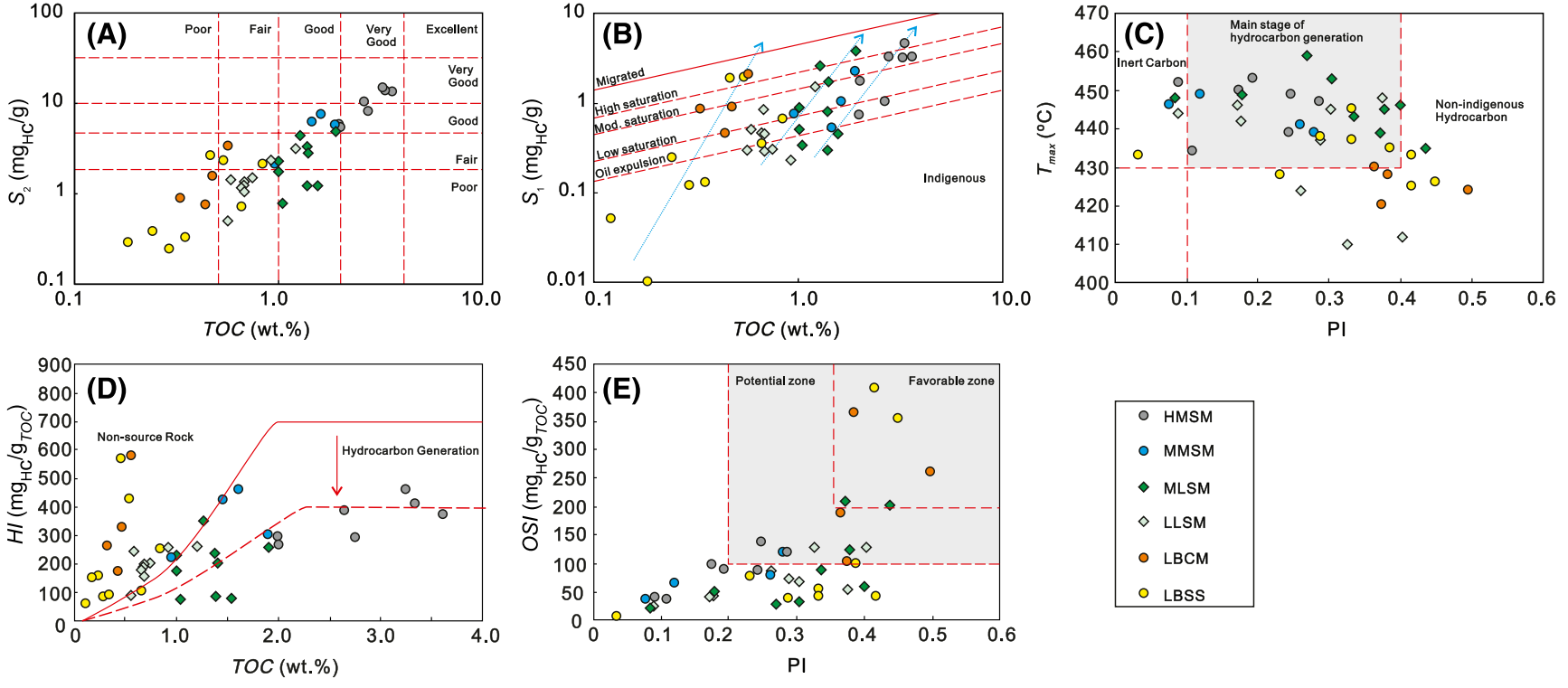

Figure 14. (A) Pyrolysis S_2 (amount of pyrolyzate released from kerogen) versus total organic carbon (*TOC*) plot showing generative source-rock potential (modified after Peters and Cassa, 1994). (B) Plot of S_1 (amount of free hydrocarbon in the sample) versus *TOC*. Values above the red line indicate migrated hydrocarbons, whereas values below the red line indicate indigenous hydrocarbons (modified after Sonnenberg et al., 2011). The three blue dotted lines represent the linear relationship between the three types of S_1 and *TOC*, respectively. (C) Plot of T_{max} (temperature of maximum hydrocarbon generation) and *PI* (production index). (D) Plot of *HI* (hydrogen index) and *TOC*. The solid red line is the relationship between the *TOC* and *HI* of the immature source rock obtained from Figure 4; the red dotted line is the relationship between the *TOC* and *HI* of the actual sample. Hydrocarbon generation caused the difference between the two lines. (E) Plot of oil saturation index (*OSI*) and *PI*. HC = hydrocarbons; HLAM = high-*TOC* laminated argillaceous mudstone; HMSM = high-*TOC* massive siliceous mudstone; LBCM = low-*TOC* bedded calcareous mudstone; LBSS = low-*TOC* bedded siliceous siltstone; LLSM = low-*TOC* laminated siliceous mudstone; MLSM = moderate-*TOC* laminated siliceous mudstone; MMSM = moderate-*TOC* massive siliceous mudstone; Mod. = moderate.

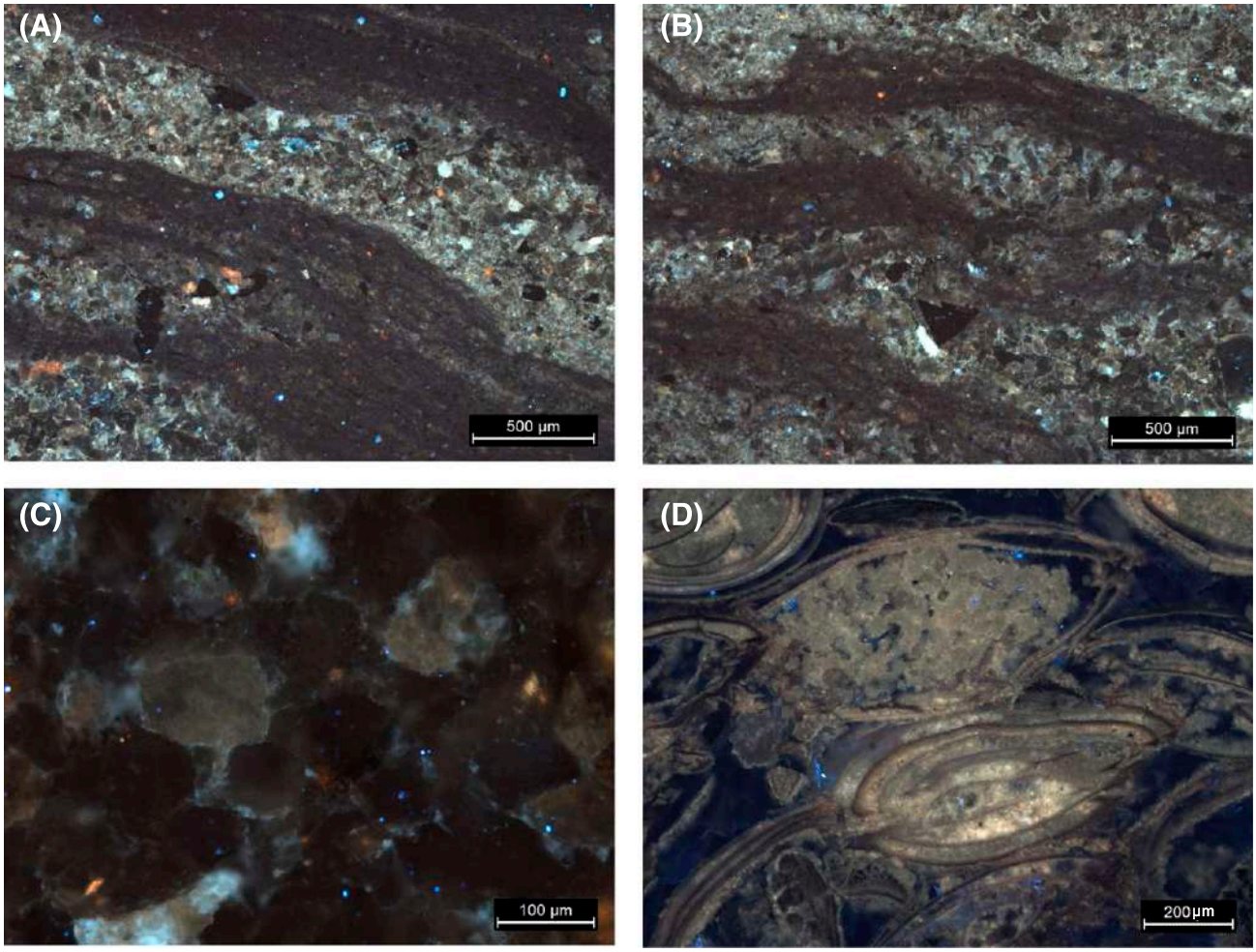

Figure 15. Fluorescence micrograph of typical lithofacies of the first member of the Qingshankou Formation. (A) Moderate–total organic carbon (*TOC*) laminated siliceous mudstone; (B) moderate-*TOC* laminated siliceous mudstone; (C) low-*TOC* bedded siliceous siltstone; (D) low-*TOC* bedded calcareous mudstone.

after generation in adjacent source rocks. This also may be caused by the fact that the argillaceous layer developed in the LLSM is not conducive to the migration of oil and gas into its interior, hence resulting in lower saturations. Both LBSS and LBCM have lower *T*OC as the denominator; furthermore, the influence of migrated bitumen that pyrolyzed as the numerator leads to higher *HI* values and *HI* and *T*OC trends that are significantly different from those seen in the source rocks (Figure 14D).

The scatter plot of *OSI* versus *PI* (Figure 14E) shows that most MLSM, LBCM, and some LBSS samples have high free shale oil contents. Some samples have *OSI* values up to 200 mg_{HC}/g_{TOC} and *PI* values of up to 0.35. This conclusion was confirmed by observation of fluorescent sheens (Figure 15). The HMSM and MMSM samples are mainly fine-grained argillaceous sedimentary rocks. Intergranular compaction makes it difficult to observe pores and fluorescence under a microscope, where the entire visual field is black. Under the MLSM microscope, dark argillaceous lamellae and light-colored silt lamellae are observed. The silty lamellae were generally light blue fluorescing, with a few showing pale yellow fluorescence (Figure 15A, B). The fluorescence intensity difference between LLSM and LBSS samples is quite large. Among the samples with higher levels of fluorescence, the light blue fluorescence mainly appeared in micropores between mineral particles (Figure 15C). The presence of isolated, semidissolved moldic porosity within shells, which is highlighted by light blue fluorescence in Figure 15D, characterizes LBCM. However, considering the extremely low hydrocarbon generation

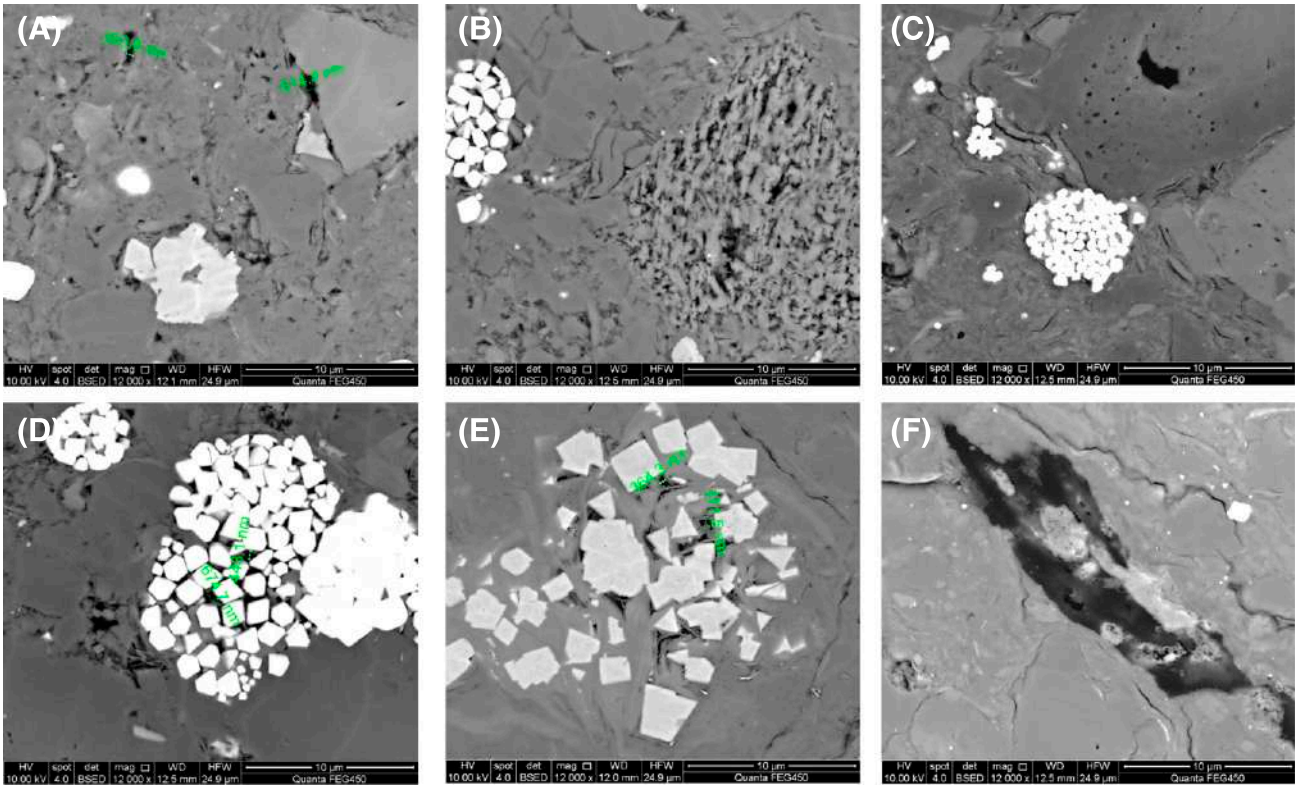

Figure 16. Field emission scanning electron microscopy images of the Qingshankou Formation shale. (A) Interparticle pores around mineral grains; (B) intraparticle pores within pyrite framboids and clay aggregates; (C) dissolution pores within feldspar; (D) intercrystalline pores within pyrite framboids; (E) interparticle pores around mineral grains; (F) organic matter pores and minor fractures. BSED = backscattered electron detector; HFW = horizontal frame width; HV = high voltage; det = detector; mag = magnification; WD = working distance.

potential of LBCM and LBSS, the *PI* of these lithofacies is still lower than that of conventional industrial oil reservoirs (nonhydrocarbon source rocks, such as sandstone reservoirs). The hydrocarbon exploration potential of LBCM and LBSS awaits further study.

Shale Oil Reservoir

The porosity and permeability of organic-rich shales are keys to the evaluation of the potential for economic production of shale oil and gas. The pores within mudstones of the study succession are of various types and sizes (Figure 16), mainly ranging in size between 150 and 620 nm. In this study, pores are classified into three major types (Loucks et al., 2012): interparticle pores between detrital or authigenic particles, intraparticle pores within detrital grains or crystals, and organic matter pores. Interparticle pores are found between particles and crystals such as quartz, feldspar, clay, and carbonate minerals (Figure 16A, C). Intraparticle pores are observed inside particles such as clays (Figure 16B), pyrite (Figure 16D), and feldspar (Figure 16C) and are caused by diagenesis and dissolution. Pyrite framboids with polyhedron-shaped intercrystalline pores are quite common in the samples (Figure 16B–D). Calcite commonly appears as a cement with rare dissolution pores. Based on the results of XRD analysis, clay minerals are dominated by illite (0–95.0 wt. %, average 67.6 wt. %), followed by an illite/smectite mixed layer (0–37.0 wt. %, average 12.8 wt. %). Illite minerals always flocculate and behave as aggregates rather than as individual particles, forming an abundance of interparticle pores between clay platelets and intraplatelet pores within clay aggregates (Figure 16B, E). Both interparticle and intraplatelet pores act as high-permeability pathways through the stratified structure of clay minerals (Slatt and O'Brien, 2011).

Organic matter pores are considered to be influenced by organic matter type and thermal maturation (Ko et al., 2016). The first member of the Qingshankou Formation contains type II organic matter, which is mainly sourced from algal–microbial mats (i.e., lamalginite; Jia et al., 2013a). Lamalginite is

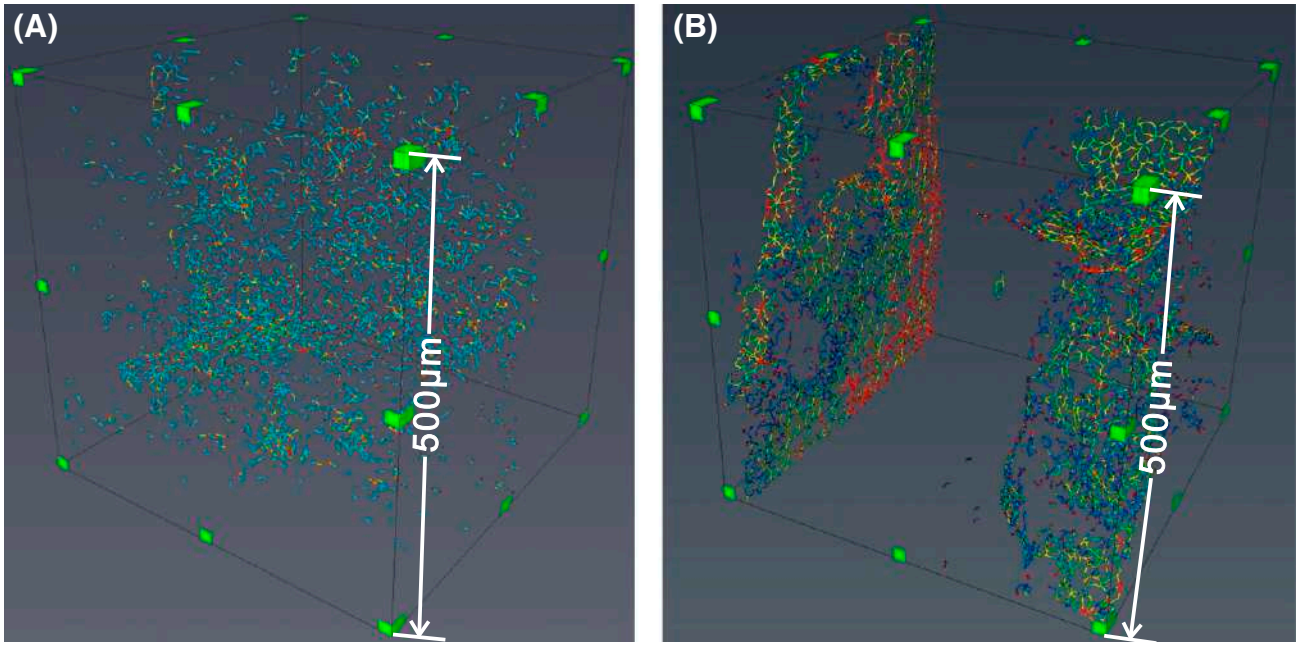

Figure 17. Three-dimensional pore network of the Qingshankou shale samples. The change of color from red to blue indicates decreasing pore size. Red represents microscopic pores, blue represents the throat, and yellow represents the transition from pores to throat. Pore network extracted from massive sample (A) and laminated sample (B), respectively.

always oriented parallel to bedding planes because of strong compaction, leading to an ellipsoidal shape of organic-matter pores with a longitudinal axis parallel to the bedding (Figure 16F). Relatively low thermal maturation (indicated by T_{max}) and type II organic matter may be reasons for the heterogeneous nature of organic-matter pores. Compared with intraparticle and interparticle pores, organic-matter pores developed in the study succession do not form a connected and effective pore network. In addition, the mineral matrix around the organic-matter particles is generally less porous, and microfracturing is observed in these locations.

Based on two-dimensional SEM observations, pore types and size distribution in the shales do not appear to be significantly different between shale lithofacies. The mineral-matrix pores dominate the shale pore types, leading to the conclusion that intraparticle pores are the main pore type in shale reservoirs in this study. As for mineral-matrix pores, Milliken et al. (2013) argued that pores developed in the mineral matrix are smaller on average, with poorer connectivity.

Three-dimensional CT scan data, however, revealed that connectivity among the different shale lithofacies differs substantially. The massive lithofacies show isolated small pores distributed randomly, implying poor connectivity (Figure 17A), whereas the laminated lithofacies have high proportions of relatively large pores (colored in red in Figure 17B) with a high probability of connectivity. Interestingly, the connected pore network is mainly observed in discrete laminae, which are preferentially composed of coarser grains. Both the size and component of particles within the different laminae control the development of reservoir space (Liu et al., 2015). The coarser-grained laminae are dominated by quartz, feldspar, and carbonates, which are beneficial to the protection of interparticle pores. Furthermore, feldspar and carbonates allow for the formation of dissolution pores. By contrast, intergranular compaction and infilling by clay minerals makes it difficult to observe pores within fine-grained laminae.

Quantitative statistics based on CT scans show that the average pore-throat size in massive mudstones is 1.93 μm, and the total pore volume is 0.86×10^6 μm^3, whereas the average pore-throat size of lamellar mudstones is 2.20 μm, and the total pore volume is 2.08×10^6 μm^3. Comparatively, the lamellar mudstones have significantly better reservoir properties than massive mudstones.

Shale Oil Potential

According to the above study, HMSM, MLSM, LBCM, and LBSS have the highest in situ hydrocarbon

saturations. However, considering a lower threshold value of 60 wt. % brittle minerals (quartz, feldspar, and carbonate) for the formation of natural fractures or to respond to hydraulic fracturing to increase permeability (Rybacki et al., 2016), HMSM and MMSM appear to be less prospective. Adding generative potential to the analysis, LBCM and LBSS show occurrences of migrated hydrocarbons from adjacent facies but poor generative potential. This implies that MLSM is more favorable than LLSM for the occurrence of higher saturations of in situ generated hydrocarbons, implying high shale oil potential.

Of the seven shale lithofacies discussed above, MLSM is proposed as being the most prospective lithofacies for shale oil because of its high generative source-rock potential, high content of indigenous hydrocarbons, high mineral brittleness index (percentage content of brittle minerals in the shales [e.g., quartz, feldspar, and carbonate; Lin et al., 2016]), and high probability of a connecting pore network. Spatial and temporal changes of lithofacies controlled by the stacking pattern within a sequence stratigraphic framework determine the distribution of prospective shale lithofacies in a sedimentary basin. Systemic investigation of the characteristics and stacking patterns of lithofacies are shown to be an effective method to allow recognition of prospective regional targets within unconventional petroleum reservoirs.

SUMMARY

The first member of the Cretaceous Qingshankou Formation is present within the Songliao Basin of northeastern China. This member was deposited in a semideep to deep lacustrine environment during a period when the lake was most extensively developed, forming the principal hydrocarbon source rocks of the Songliao Basin. The *TOC* of the Qingshankou shale ranges from 0.12 to 3.62 wt. % (average 1.18 wt. %). The *HI* values range from 57 to 582 mg_{HC}/g_{TOC} (average 253 mg_{HC}/g_{TOC}), corresponding to the presence of kerogen types II and III. The organic matter maturity is within the main stage of oil generation (average T_{max} 439°C). The mineralogy of these sedimentary rocks is dominated by quartz, plagioclase, clay, carbonates, and K-feldspar, plotting in the area of siliceous mudstones in ternary plots. The *TOC* and bedding correlate well to the total clay content, suggesting mechanical sedimentary differentiation dominates the process of organic matter enrichment.

Seven types of shale lithofacies were identified based on the analysis of *TOC*, rock fabric, and mineral composition, exhibiting rapid vertical and lateral changes controlled by depositional setting and evolution. Filling sequences composed of different lithofacies characterized by increasing *TOC* and total clay content and decreasing layer thickness (i.e., from bedded to laminated then to massive sedimentary structures) represent an overall trend from a shallow-water to a deep-water depositional environment. In the case where a reversed stratigraphic sequence is observed, this is interpreted as representative of a depositional environment that progressed from a deep to a shallow lake setting. Stacking patterns from bottom to top in a transgressive, short-term cycle consist of LBSS or LBCM, LLSM, MLSM, MMSM, HMSM, and HLAM. The vertical lithofacies variations define three complete short-term cycles in the studied section, with transgressive and regressive system tracts in each cycle. Spatial distribution of lithofacies of the first member of the Qingshankou Formation is controlled in the vertical sense by sedimentary evolution and terrigenous input variations in the lateral sense.

For self-sourced shale oil, MLSM is proposed as being the most favorable lithofacies because of its high generative source-rock potential, high content of indigenous hydrocarbons, high mineral brittleness index, and high probability of a connecting pore network. Systemic investigation of the characteristics and stacking patterns of lithofacies would be an effective method to allow recognition of prospective regional targets in unconventional petroleum reservoir settings.

REFERENCES CITED

Abouelresh, M. O., and R. M. Slatt, 2012, Lithofacies and sequence stratigraphy of the Barnett Shale in east-central Fort Worth Basin, Texas: AAPG Bulletin, v. 96, no. 1, p. 1–22, doi:10.1306j/04261110116.

Allix, P., A. Burnham, T. Fowler, M. Herron, R. Kleinberg, and B. Symington, 2010, Coaxing oil from shale: Oilfield Review, v. 22, no. 4, p. 4–15.

Anderson, T., 2014, Key parameters for liquid-rich unconventional plays: Case studies from North America: AAPG Search and Discovery article 80354, accessed August 28, 2018, http://www.searchanddiscovery.com/pdfz/documents/2014/80354anderson/ndx_anderson.pdf.html.

Aplin, A. C., and J. H. S. Macquaker, 2011, Mudstone diversity: Origin and implications for source, seal, and reservoir properties in petroleum systems: AAPG Bulletin, v. 95, no. 12, p. 2031–2059, doi:10.1306/03281110162.

Bechtel, A., J. Jia, S. A. I. Strobl, R. F. Sachsenhofer, Z. Liu, R. Gratzer, and W. Püttmann, 2012, Palaeoenvironmental conditions during deposition of the Upper Cretaceous oil shale sequences in the Songliao Basin (NE China): Implications from geochemical analysis: Organic Geochemistry, v. 46, p. 76–95, doi:10.1016/j.orggeochem.2012.02.003.

Bissada, K. K., 1982, Geochemical constraints on petroleum generation and migration—A review: Proceedings of the Second Association of Southeast Asian Nations Council on Petroleum Conference and Exhibition, Manila, Philippines, October 7–11, 1981, p. 69–95, doi:S0264-8172(14)00042-7/sref2.

Bruhn, C. H. L., 1999, Reservoir architecture of deep-lacustrine sandstones from the Early Cretaceous Recôncavo rift basin, Brazil: AAPG Bulletin, v. 83, no. 9, p. 1502–1525, doi:10.1306/E4FD41F7-1732-11D7-8645000102C1865D.

Campbell, C. V., 1967, Lamina, laminaset, bed and bedset: Sedimentology, v. 8, no. 1, p. 7–26, doi:10.1111/j.1365-3091.1967.tb01301.x.

Cao, H., Y.-R. Zou, Y. Lei, D. Xi, X. Wan, and P. Peng, 2017, Shale oil assessment for the Songliao Basin, northeastern China, using oil generation–sorption method: Energy & Fuels, v. 31, no. 5, p. 4826–4842, doi:10.1021/acs.energyfuels.7b00098.

Chen, S., Y. Zhu, H. Wang, H. Liu, W. Wei, and J. Fang, 2011, Shale gas reservoir characterisation: A typical case in the southern Sichuan Basin of China: Energy, v. 36, no. 11, p. 6609–6616, doi:10.1016/j.energy.2011.09.001.

Demaison, G. J., and G. T. Moore, 1980, Anoxic environments and oil source bed genesis: Organic Geochemistry, v. 2, no. 1, p. 9–31, doi:10.1016/0146-6380(80)90017-0.

Dill, H. G., R.-R. Ludwig, A. Kathewera, and J. Mwenelupembe, 2005, A lithofacies terrain model for the Blantyre Region: Implications for the interpretation of palaeosavanna depositional systems and for environmental geology and economic geology in southern Malawi: Journal of African Earth Sciences, v. 41, p. 341–393, doi:10.1016/j.jafrearsci.2005.07.005.

Dyni, J. R., 2003, Geology and resources of some world oil-shale deposits: Oil Shale, v. 20, no. 3, p. 193–252.

Eberl, D. D., 2003, User's guide to RockJock—A program for determining quantitative mineralogy from powder x-ray diffraction data: Washington, DC, US Geological Survey Open-File Report 2003-78, 47 p.

Eberzin, A. G., 1940, Middle and upper Pliocene of the Black Sea region, *in* Statigrafiya SSSR: Neogene SSSR (Stratigraphy of the USSR: Neogene of the USSR): Moscow, Doklady Akademii Nauk SSSR, v. 8, p. 477–566.

Espitalié, J., M. Madec, B. P. Tissot, J. J. Mennig, and P. Leplat, 1977, Source rock characterization method for petroleum exploration: Offshore Technology Conference, Houston, Texas, May 2–5, 1977, p. 439–444, doi:10.4043/2935-ms.

Espitalié, J., F. Marquis, and I. Barsony, 1984, Geochemical logging, *in* K. J. Voorhees, ed., Analytical pyrolysis: Techniques and applications: Boston, Butterworths, p. 276–304, doi:10.1016/B978-0-408-01417-5.50013-5.

Feng, Z., W. Fang, Z. Li, X. Wang, Q. Huo, C. Huang, J. Zhang, and H. Zeng, 2011, Depositional environment of terrestrial petroleum source rocks and geochemical indicators in the Songliao Basin: Science China Earth Sciences, v. 54, no. 9, p. 1304–1317, doi:10.1007/s11430-011-4268-0.

Feng, Z., C. Jia, X. Xie, S. Zhang, Z. Feng, and T. A. Cross, 2010, Tectonostratigraphic units and stratigraphic sequences of the nonmarine Songliao basin, northeast China: Basin Research, v. 22, no. 1, p. 79–95, doi:10.1111/j.1365-2117.2009.00445.x.

Gamero-Diaz, H., C. K. Miller, and R. Lewis, 2013, sCore: A mineralogy based classification scheme for organic mudstones: Society of Petroleum Engineers Annual Technical Conference and Exhibition, New Orleans, Louisiana, September 30–October 2, 2013, 17 p., doi:10.2118/166284-MS.

Gierlowski-Kordesch, E., 2010, Lacustrine carbonates, *in* A. M. Alonso-Zarza and L. H. Tanner, eds., Carbonates in continental settings: facies, environments, and processes, p. 1–101, 10.1016/S0070-4571(09)06101-9.

Heath, J. E., T. A. Dewers, B. J. O. L. McPherson, R. Petrusak, T. C. Chidsey, A. J. Rinehart, and P. S. Mozley, 2011, Pore networks in continental and marine mudstones: Characteristics and controls on sealing behavior: Geosphere, v. 7, no. 2, p. 429–454, doi:10.1130/GES00619.1.

Huang, Y., G. Yang, J. Gu, P. Wang, Q. Huang, Z. Feng, and L. Feng, 2013, Marine incursion events in the Late Cretaceous Songliao Basin: Constraints from sulfur geochemistry records: Palaeogeography, Palaeoclimatology, Palaeoecology, v. 385, p. 152–161, doi:10.1016/j.palaeo.2013.03.017.

Jarvie, D. M., 2012, Shale resource systems for oil and gas: Part 2—Shale-oil resource systems, *in* J. A. Breyer, ed., Shale reservoirs—Giant resources for the 21st century: AAPG Memoir 97, p. 89–119, doi:10.1306/13321447M973489.

Jarvie, D. M., R. J. Hill, T. E. Ruble, and R. M. Pollastro, 2007, Unconventional shale-gas systems: The Mississippian Barnett Shale of north-central Texas as one model for thermogenic shale-gas assessment: AAPG Bulletin, v. 91, no. 4, p. 475–499, doi:10.1306/12190606068.

Jia, J., A. Bechtel, Z. Liu, S. A. I. Strobl, P. Sun, and R. F. Sachsenhofer, 2013a, Oil shale formation in the Upper Cretaceous Nenjiang Formation of the Songliao Basin (NE China): Implications from organic and inorganic geochemical analyses: International Journal of Coal Geology, v. 113, p. 11–26, doi:10.1016/j.coal.2013.03.004.

Jia, J., Z. Liu, A. Bechtel, S. A. I. Strobl, and P. Sun, 2013b, Tectonic and climate control of oil shale deposition in the Upper Cretaceous Qingshankou Formation (Songliao Basin, NE China): International Journal of Earth

Sciences, v. 102, no. 6, p. 1717–1734, doi:10.1007/s00531-013-0903-7.

Katz, B. J., 2001, Lacustrine basin hydrocarbon exploration – Current thoughts: Journal of Paleolimnology, v. 26, no. 2, p. 161–179, doi:10.1023/A:1011173805661.

Katz, B., and F. Lin, 2014, Lacustrine basin unconventional resource plays: Key differences: Marine and Petroleum Geology, v. 56, p. 255–265, doi:10.1016/j.marpetgeo.2014.02.013.

Ko, L. T., R. G. Loucks, T. Zhang, S. C. Ruppel, and D. Shao, 2016, Pore and pore network evolution of Upper Cretaceous Boquillas (Eagle Ford-equivalent) mudrocks: Results from gold tube pyrolysis experiments: AAPG Bulletin, v. 100, no. 11, p. 1693–1722, doi:10.1306/04151615092.

Langford, F. F., and M. M. Blanc-Valleron, 1990, Interpreting Rock-Eval pyrolysis data using graphs of pyrolizable hydrocarbons versus total organic carbon: AAPG Bulletin, v. 74, no. 6, p. 799–804, doi:10.1306/0C9B238F-1710-11D7-8645000102C1865D.

Lazar, O. R., K. M. Bohacs, J. H. S. Macquaker, J. Schieber, and T. M. Demko, 2015, Capturing key attributes of fine-grained sedimentary rocks in outcrops, cores, and thin sections: Nomenclature and description guidelines: Journal of Sedimentary Research, v. 85, no. 3, p. 230–246, doi:10.2110/jsr.2015.11.

Lenoir, N., M. Bornert, J. Desrues, P. Bésuelle, and G. Viggiani, 2007, Volumetric digital image correlation applied to x-ray microtomography images from triaxial compression tests on argillaceous rock: Strain, v. 43, no. 3, p. 193–205, doi:10.1111/j.1475-1305.2007.00348.x.

Li, D., R. Jiang, and B. J. Katz, 1994, Petroleum generation in the nonmarine Qingshankou Formation (Lower Cretaceous), Songliao Basin, China, *in* B. J. Katz, ed., Petroleum source rocks: Berlin, Springer-Verlag, p. 131–148.

Li, T., Z. Jiang, C. Xu, B. Liu, G. Liu, P. Wang, X. Li, W. Chen, C. Ning, and Z. Wang, 2017a, Effect of pore structure on shale oil accumulation in the lower third member of the Shahejie formation, Zhanhua Sag, eastern China: Evidence from gas adsorption and nuclear magnetic resonance: Marine and Petroleum Geology, v. 88, p. 932–949, doi:10.1016/j.marpetgeo.2017.09.030.

Li, T., Z. Jiang, C. Xu, Y. Yuan, P. Wang, G. Liu, B. Zhang, C. Ning, and Z. Wang, 2017b, Effect of sedimentary environment on shale lithofacies in the lower third member of the Shahejie Formation, Zhanhua Sag, eastern China: Interpretation, v. 5, no. 4, p. T487–T501, doi:10.1190/INT-2017-0016.1.

Lin, D., T. Zhang, J. Liao, M. Liao, D. Geng, X. Ren, and Y. Chen, 2016, Mineral composition and brittleness analysis of organic-rich Lower Paleozoic shale in south Sichuan and north Yunnan areas of China: Chemistry and Technology of Fuels and Oils, v. 52, no. 2, p. 218–223, doi:10.1007/s10553-016-0693-2.

Liu, B., A. Bechtel, D. Gross, X. Fu, X. Li, and R. F. Sachsenhofer, 2018, Middle Permian environmental changes and shale oil potential evidenced by high-resolution organic petrology, geochemistry and mineral composition of the sediments in the Santanghu Basin, Northwest China: International Journal of Coal Geology, v. 185, p. 119–137, doi:10.1016/j.coal.2017.11.015.

Liu, B., A. Bechtel, R. F. Sachsenhofer, D. Gross, R. Gratzer, and X. Chen, 2017, Depositional environment of oil shale within the second member of Permian Lucaogou Formation in the Santanghu Basin, Northwest China: International Journal of Coal Geology, v. 175, p. 10–25, doi:10.1016/j.coal.2017.03.011.

Liu, B., J. He, Y. Lü, Q. Ran, C. Dai, and M. Li, 2014a, Parameters and method for shale oil assessment: Taking Qingshankou Formation shale oil of Northern Songliao Basin (in Chinese): Journal of Central South University, v. 45, no. 11, p. 3846–3852.

Liu, B., Y. Lü, Y. Meng, X. Li, X. Guo, Q. Ma, and W. Zhao, 2015, Petrologic characteristics and genetic model of lacustrine lamellar fine-grained rock and its significance for shale oil exploration: A case study of Permian Lucaogou Formation in Malang sag, Santanghu Basin, NW China: Petroleum Exploration and Development, v. 42, no. 5, p. 656–666, doi:10.1016/S1876-3804(15)30060-4.

Liu, B., Y. Lü, Q. Ran, C. Dai, M. Li, and M. Wang, 2014b, Geological conditions and exploration potential of shale oil in Qingshankou Formation, Northern Songliao Basin (in Chinese): Oil and Gas Geology, v. 35, no. 2, p. 280–285, doi:10.11743/ogg20140216.

Liu, C., Z. Wang, Z. Guo, W. Hong, C. Dun, X. Zhang, B. Li, and L. Wu, 2017, Enrichment and distribution of shale oil in the Cretaceous Qingshankou Formation, Songliao Basin, Northeast China: Marine and Petroleum Geology, v. 86, p. 751–770, doi:10.1016/j.marpetgeo.2017.06.034.

Liu, Z. J., D. P. Wang, L. Liu, W. Z. Liu, P. J. Wang, X. D. Du, and G. Yang, 1993, Sedimentary characteristics of the Cretaceous in the Songliao Basin: Acta Geologica Sinica, v. 6, no. 2, p. 167–180, doi:10.1111/j.1755-6724.1993.mp6002005.x.

Loucks, R. G., R. M. Reed, S. C. Ruppel, and U. Hammes, 2012, Spectrum of pore types and networks in mudrocks and a descriptive classification for matrix-related mudrock pores: AAPG Bulletin, v. 96, no. 6, p. 1071–1098, doi:10.1306/08171111061.

Loucks, R. G., R. M. Reed, S. C. Ruppel, and D. M. Jarvie, 2009, Morphology, genesis, and distribution of nanometer-scale pores in siliceous mudstones of the Mississippian Barnett Shale: Journal of Sedimentary Research, v. 79, no. 12, p. 848–861, doi:10.2110/jsr.2009.092.

Loucks, R. G., and S. C. Ruppel, 2007, Mississippian Barnett Shale: Lithofacies and depositional setting of a deep-water shale-gas succession in the Fort Worth Basin, Texas: AAPG Bulletin, v. 91, no. 4, p. 579–601, doi:10.1306/11020606059.

Ma, Y., M. Fan, Y. Lu, H. Liu, Y. Hao, Z. Xie, Z. Liu, L. Peng, X. Du, and H. Hu, 2016, Climate-driven paleolimnological change controls lacustrine mudstone depositional process and organic matter accumulation: Constraints from lithofacies and geochemical studies in the Zhanhua Depression, eastern China: International Journal of Coal Geology, v. 167, p. 103–118, doi:10.1016/j.coal.2016.09.014.

Macquaker, J. H. S., and A. E. Adams, 2003, Maximizing information from fine-grained sedimentary rocks: An inclusive nomenclature for mudstones: Journal of Sedimentary Research, v. 73, no. 5, p. 735–744, doi:10.1306/012203730735.

Milliken, K. L., M. Rudnicki, D. N. Awwiller, and T. Zhang, 2013, Organic matter-hosted pore system, Marcellus Formation (Devonian), Pennsylvania: AAPG Bulletin, v. 97, no. 2, p. 177–200, doi:10.1306/07231212048.

Newport, L. P., A. C. Aplin, J. G. Gluyas, H. C. Greenwell, and D. R. Gröcke, 2016, Geochemical and lithological controls on a potential shale reservoir: Carboniferous Holywell Shale, Wales: Marine and Petroleum Geology, v. 71, p. 198–210, doi:10.1016/j.marpetgeo.2015.11.026.

Peters, K. E., and M. R. Cassa, 1994, Applied source rock geochemistry: Chapter 5: Part II. Essential elements, *in* L. B. Magoon and W. G. Dow, eds., The petroleum system–From source to trap: AAPG Memoir 60, p. 93–120, doi:10.1306/M60585C5.

Rickman, R., M. J. Mullen, J. E. Petre, W. V. Grieser, and D. Kundert, 2008, A practical use of shale petrophysics for stimulation design optimization: All shale plays are not clones of the Barnett Shale: Society of Petroleum Engineers Annual Technical Conference and Exhibition, Denver, Colorado, September 21–24, 2008, 11 p., doi:10.2118/115258-MS.

Rybacki, E., T. Meier, and G. Dresen, 2016, What controls the mechanical properties of shale rocks?—Part II: Brittleness: Journal of Petroleum Science and Engineering, v. 144, p. 39–58, doi:10.1016/j.petrol.2016.02.022.

Schieber, J., and J. B. Southard, 2009, Bedload transport of mud by floccule ripples—Direct observation of ripple migration processes and their implications: Geology, v. 37, no. 6, p. 483–486, doi:10.1130/G25319A.1.

Schieber, J., and Z. Yawar, 2009, New twist on mud deposition – Mud ripples in experiment and rock record: The Sedimentary Record, v. 7, no. 2, p. 4–8, doi:10.2110/sedred.2009.2.4.

Schmoker, J. W., 1981, Determination of organic-matter content of Appalachian Devonian Shale from gamma-ray logs: AAPG Bulletin, v. 65, no. 7, p. 1285–1298, doi:10.1306/03B5949A-16D1-11D7-8645000102C1865D.

Shi, L., Z. Wang, G. Zhang, Y. Zhang, and E. Xing, 2015, Distribution and formation of tight oil in Qijia area, Songliao Basin, NE China: Petroleum Exploration and Development, v. 42, no. 1, p. 48–55, doi:10.1016/S1876-3804(15)60005-2.

Slatt, R. M., and N. R. O'Brien, 2011, Pore types in the Barnett and Woodford gas shales: Contribution to understanding gas storage and migration pathways in fine-grained rocks: AAPG Bulletin, v. 95, no. 12, p. 2017–2030, doi:10.1306/03301110145.

Slatt, R. M., and N. D. Rodriguez, 2012, Comparative sequence stratigraphy and organic geochemistry of gas shales: Commonality or coincidence?: Journal of Natural Gas Science and Engineering, v. 8, p. 68–84, doi:10.1016/j.jngse.2012.01.008.

Sonnenberg, S. A., H. Jin, and J. F. Sarg, 2011, Bakken mudrocks of the Williston Basin, world class source rocks: AAPG Search and Discovery article 80171, accessed August 28, 2018, http://www.searchanddiscovery.com/documents/2011/80171sonnenberg/ndx_sonnenberg.pdf.

Tang, X., Z. Jiang, H. Huang, S. Jiang, L. Yang, F. Xiong, L. Chen, and J. Feng, 2016, Lithofacies characteristics and its effect on gas storage of the Silurian Longmaxi marine shale in the southeast Sichuan Basin, China: Journal of Natural Gas Science and Engineering, v. 28, p. 338–346, doi:10.1016/j.jngse.2015.12.026.

Tyson, R. V., R. C. L. Wilson, and C. Downie, 1979, A stratified water column environmental model for the type Kimmeridge Clay: Nature, v. 277, no. 5695, p. 377–380, doi:10.1038/277377a0.

Wang, F., W. Feng, J. Guan, and Z. He, 2016, Geochemical assessment of lacustrine tight oil and application (in Chinese): Journal of Jilin University, v. 46, no. 2, p. 388–397, doi:10.13278/j.cnki.jjuese.201602108.

Wang, G., and T. R. Carr, 2012, Methodology of organic-rich shale lithofacies identification and prediction: A case study from Marcellus Shale in the Appalachian basin: Computers & Geosciences, v. 49, p. 151–163, doi:10.1016/j.cageo.2012.07.011.

Wang, P., F. Mattern, N. A. Didenko, D. Zhu, B. Singer, and X. Sun, 2016, Tectonics and cycle system of the Cretaceous Songliao Basin: An inverted active continental margin basin: Earth-Science Reviews, v. 159, p. 82–102, doi:10.1016/j.earscirev.2016.05.004.

Wei, H., J. Liu, and Q. Meng, 2010, Structural and sedimentary evolution of the southern Songliao Basin, northeast China, and implications for hydrocarbon prospectivity: AAPG Bulletin, v. 94, no. 4, p. 531–564, doi:10.1306/09080909060.

Wu, H., S. Zhang, G. Jiang, L. Hinnov, T. Yang, H. Li, X. Wan, and C. Wang, 2013, Astrochronology of the Early Turonian-Early Campanian terrestrial succession in the Songliao Basin, northeastern China and its implication for long-period behavior of the Solar System: Palaeogeography, Palaeoclimatology, Palaeoecology, v. 385, p. 55–70, doi:10.1016/j.palaeo.2012.09.004.

Xi, K., Y. Cao, J. Jahren, R. Zhu, K. Bjørlykke, B. G. Haile, L. Zheng, and H. Hellevang, 2015, Diagenesis and reservoir quality of the Lower Cretaceous Quantou Formation tight sandstones in the southern Songliao Basin, China: Sedimentary Geology, v. 330, p. 90–107, doi:10.1016/j.sedgeo.2015.10.007.

Xu, J., A. Bechtel, R. F. Sachsenhofer, Z. Liu, R. Gratzer, Q. Meng, and Y. Song, 2015, High resolution geochemical analysis of organic matter accumulation in the Qingshankou Formation, Upper Cretaceous, Songliao Basin (NE China): International Journal of Coal Geology, v. 141–142, p. 23–32, doi:10.1016/j.coal.2015.03.003.

Zhao, B., C. Wang, X. Wang, and Z. Feng, 2013, Late Cretaceous (Campanian) provenance change in the Songliao Basin, NE China: Evidence from detrital zircon U-Pb ages from the Yaojia and Nenjiang Formations: Palaeogeography, Palaeoclimatology, Palaeoecology, v. 385, p. 83–94, doi:10.1016/j.palaeo.2012.03.017.

Zhao, B., C. Wang, X. Wang, and Z. Feng, 2015, Corrigendum to "Late Cretaceous (Campanian) provenance change in the Songliao Basin, NE China: Evidence from detrital zircon U-Pb ages from the Yaojia and Nenjiang Formations": [[Palaeogeogr. Palaeoclimatol. Palaeoecol. 385C (2013) 83–94]] Palaeogeography, Palaeoclimatology, Palaeoecology, v. 430, p. 132, doi:10.1016/j.palaeo.2015.03.040.

Zhong, Q., and W. Yang, 1978, About Songliao Basin characterization of structural development (in Chinese): Petroleum Exploration and Development, v. 5, p. 50–52.

Zhou, Y., and R. Littke, 1999, Numerical simulation of the thermal maturation, oil generation and migration in the Songliao Basin, Northeastern China: Marine and Petroleum Geology, v. 16, no. 8, p. 771–792, doi:10.1016/S0264-8172(99)00043-4.

Zhu, X., H. Zeng, S. Li, Y. Dong, S. Zhu, D. Zhao, and W. Huang, 2017, Sedimentary characteristics and seismic geomorphologic responses of a shallow-water delta in the Qingshankou Formation from the Songliao Basin, China: Marine and Petroleum Geology, v. 79, p. 131–148, doi:10.1016/j.marpetgeo.2016.09.018.